



INSTITUT DE FRANCE
Académie des sciences

Comptes Rendus

Chimie

Dominique Bazin, Elise Boudierlique, Ellie Tang, Michel Daudon,
Jean-Philippe Haymann, Vincent Frochet, Emmanuel Letavernier,
Els Van de Perre, James C. Williams Jr., James E. Lingeman
and Ferenc Borondics

**Using mid infrared to perform investigations beyond the diffraction
limits of microcrystalline pathologies: advantages and limitation of
Optical PhotoThermal IR spectroscopy**


Volume 25, Special Issue S1 (2022), p. 105-131

Published online: 27 July 2022

<https://doi.org/10.5802/crchim.196>

Part of Special Issue: Microcrystalline pathologies: Clinical issues and
nanochemistry

Guest editors: Dominique Bazin (Université Paris-Saclay, CNRS, ICP, France),
Michel Daudon, Vincent Frochet, Emmanuel Letavernier and Jean-Philippe
Haymann (Sorbonne Université, INSERM, AP-HP, Hôpital Tenon, France)

 This article is licensed under the
CREATIVE COMMONS ATTRIBUTION 4.0 INTERNATIONAL LICENSE.
<http://creativecommons.org/licenses/by/4.0/>



*Les Comptes Rendus. Chimie sont membres du
Centre Mersenne pour l'édition scientifique ouverte*
www.centre-mersenne.org
e-ISSN : 1878-1543



Microcrystalline pathologies: Clinical issues and nanochemistry / *Pathologies microcristallines : questions cliniques et nanochimie*

Using mid infrared to perform investigations beyond the diffraction limits of microcrystalline pathologies: advantages and limitation of Optical PhotoThermal IR spectroscopy

Dominique Bazin^{*, a, b}, Elise Boudierlique^{c, d}, Ellie Tang^{c, d}, Michel Daudon^{c, d, e}, Jean-Philippe Haymann^{c, d, e}, Vincent Frochot^{c, d, e}, Emmanuel Letavernier^{c, d, e}, Els Van de Perre^f, James C. Williams Jr.^g, James E. Lingeman^h and Ferenc Borondicsⁱ

^a Institut de Chimie Physique, UMR CNRS 8000, Bâtiment 350, Université Paris Saclay, 91405 Orsay cedex, France

^b Laboratoire de Physique des Solides, UMR CNRS 8502, Bâtiment 510, Université Paris-Sud, 91405 Orsay cedex, France

^c Sorbonne Universités, UPMC Univ Paris 06, UMR S 702, Paris, France

^d INSERM, UMR S 1155, Paris, France

^e Explorations fonctionnelles multidisciplinaires, AP-HP, Hôpital Tenon, Paris, France

^f Vrije Universiteit Brussel (VUB), Universitair Ziekenhuis Brussel (UZ Brussel), Nephrology Department, Brussels, Belgium

^g Department of Anatomy, Cell Biology & Physiology, Indiana University School of Medicine, Indianapolis, Indiana, USA

^h Department of Urology, Indiana University School of Medicine, Indianapolis, Indiana, USA

ⁱ Synchrotron SOLEIL, L'Orme des Merisiers, Saint-Aubin, BP 48, 91192 Gif-sur-Yvette, France

E-mails: dominique.bazin@universite-paris-saclay.fr (D. Bazin), elise.boudierlique@inserm.fr (E. Boudierlique), Ellieyali.tang@hotmail.com (E. Tang), daudonmichel24@gmail.com (M. Daudon), Jean-philippe.haymann@aphp.fr (J.-P. Haymann), vincent.frochot@aphp.fr (V. Frochot), emmanuel.letavernier@aphp.fr (E. Letavernier), Els.VandePerre@uzbrussel.be (E. Van de Perre), jwillia3@iu.edu (J. C. Williams, Jr.), J.Lingeman@IUHealth.org (J. E. Lingeman), ferenc.borondics@synchrotron-soleil.fr (F. Borondics)

* Corresponding author.

Abstract. Understanding the physico-chemistry related to crystalline pathologies constitutes a challenge in several medical specialties such as nephrology, dermatology or oncology. Regarding nephrology, the chemical diversity of concretions such as kidney stones calls for characterization techniques to determine the chemical composition of concretions. The starting point of this contribution is given by Fourier Transform InfraRed (FTIR) spectroscopy which is routinely used at the hospital to determine the chemical composition of kidney stones as well as ectopic calcifications present in kidney biopsy. For kidney stones, the quantity of sample is sufficient to perform a significant analysis through classical FTIR. For ectopic calcifications, μ FTIR can be inefficient in the case of μ calcification in the tissue when their size is less than 10 μ m. For such samples, Optical PhotoThermal IR (OPT-IR) spectroscopy may constitute a way to overcome this experimental difficulty through the acquisition of IR spectrum with a spatial resolution close to 500 nm.

To illustrate such opportunity, we first compare the IR spectrum acquired with a classical experimental set-up related to classical IR spectroscopy to IR spectrum collected with a OPT-IR one for different compounds namely calcium oxalate monohydrate, calcium oxalate dehydrate, calcium phosphate apatite and magnesium ammonium phosphate hexahydrate. Such comparison helps us to assess specificity of OPT-IR. Then, we consider several pathological calcifications associated to hyperoxaluria, adenine phosphoribosyltransferase (APRT) deficiency or the presence of Randall's plaque. We will see that the nanometer spatial resolution constitutes a major advantage versus a micrometre one. Also, in the case of Randall's plaque, we show that OPT-IR can determine the chemical composition of microscopic concretion without any kind of preparation. Such experimental fact is clearly a major advantage. Finally, we also extended this first investigation in nephrology by considering breast calcifications. In that case, if the number of chemical phases is quite low compared to the number of chemical phases identified in ectopic calcifications present in kidney (four instead of 24), the challenge is related to the possibility to distinguish between the different calcium phosphate namely amorphous carbonated calcium phosphate, CA and whitlockite.

The complete set of data indicates the limitations and the advantages of OPT-IR spectroscopy.

Keywords. PhotoThermal IR spectroscopy, Pathological calcifications, Randall's plaque, Kidney stones, Breast calcifications, Kidney biopsy.

Published online: 27 July 2022

1. Introduction

An analysis of the medical literature indicates clearly an ubiquity of microcrystalline pathologies [1–7] in human which encompass several major diseases such as cancer [8–10], cardiovascular [11–13], infection [14–19] as well as genetic [20–26] disorders. It should be kept in mind that abnormal deposits in human tissues may have endogenous as well as exogenous origin [27–29].

Among the different microcrystalline pathologies [1–7], urolithiasis is probably the most popular. Epidemiological surveys of urolithiasis have shown that in economically developed countries the prevalence rate ranged between 4% and 20% [30–33]. As noticed by Trinchieri [34], in the latter part of the 20th century prevalence and incidence of upper urinary tract stones were still increasing in Western countries probably resulting from improvements in clinical-diagnostic procedures and changes in nutritional and environmental factors.

In the service des explorations fonctionnelles of the Tenon hospital, 3000 kidney stones are analyzed

each year following the morpho-constitutional stone analysis described four decades ago [35–41]. In short, the standardized protocol comprises two steps:

- First, a stereomicroscope (magnification $\times 10$ –40) is used to examine the surface and section of the calculus, with the identification of the nucleus (or core) and to observe the inner organization. For each stone, the size, the form, the color, the aspect (smooth, rough or spiky) of the surface, the presence of a papillary imprint (umbilication), the presence of Randall's plaque, the aspect of the section (well organized with concentric layers and/or radiating organization, or poorly organized and loose structure) and location and aspect of the nucleus is considered.
- Second, an analysis is performed by Fourier Transform InfraRed (FTIR) [42–45] of a sample of each part of the calculus (nucleus, mid-section and surface), whenever allowed by the size of the stone, and in all cases, the determination of the global proportion of com-

ponents in a powdered sample of the whole stone [46–49].

Such physicochemical information leads to a medical diagnosis for the clinician. For kidney stones, the amount of samples is sufficient to perform classical FTIR experiments. Also, other parameters have to be considered such as the price of the apparatus as well as the facility to handle experiments. All these points lead to the fact that for kidney stones, it is not necessary to use micro and nano IR spectroscopies.

The challenge lies in the identification of chemical compounds present in pathological microcrystalline deposits (PMCD). It is of clinical importance to accurately identify crystals found in the tissue as soon as possible. Figure 1 presents a typical set of data which can be obtained through classical μ FTIR spectroscopy. Here, FTIR hyperspectral images were recorded with a Spectrum Spotlight 400 FTIR imaging system (Perkin Elmer Life Sciences, France), with a spectral resolution of 8 cm^{-1} . Each spectral image, covering the biopsy, consisted of about 30,000 spectra. A precise identification of PMCD is straightforward through the position of characteristic IR absorption bands.

The two primary features due to proteins (Figure 1c), are the amide I ($1600\text{--}1700\text{ cm}^{-1}$) and amide II ($1500\text{--}1560\text{ cm}^{-1}$) bands, which arise primarily from the C–O and C–N stretching vibrations of the peptide bond, respectively [14]. Apart from these contributions, IR absorption bands of calcium oxalate monohydrate (COM) positioned at 780 cm^{-1} (black arrow in Figure 1c) or at 1314 cm^{-1} (red arrow in Figure 1c) may be selected to obtain the spatial distribution of COM crystallites within the biopsy.

One drawback is that IR spectroscopy needs a data bank in which spectra of chemical compounds are gathered to compare them to the IR spectra collected from the sample [50]. In the case of the presence of a chemical compound with unknown crystallographic structure in the chemical composition of an abnormal deposit, X-ray scattering constitutes a more valuable technique [51–53].

In most clinical cases, μ FTIR spectroscopy is able to characterize microcrystals present in kidney biopsies [49,54]. Such measurements are also performed at Tenon hospital. Let's just recall that at the Tenon Hospital, more than 85,000 kidney stones have been

analysed by FTIR spectroscopy, as well as more than 2000 biological tissues, including more than 1600 kidney biopsies [4,54,55].

Unfortunately, one limitation of μ FTIR lies in its lateral spatial resolution. The diffraction of the long mid-IR wavelengths ($2.5\text{ }\mu\text{m}\text{--}25\text{ }\mu\text{m}$) limits the lateral resolution of IR microscopy to several micrometers [56,57]. More precisely, this lateral resolution R_L is given by the relationship:

$$R_L = 0.61\lambda/nNA$$

where λ is the wavelength, n is the index of refraction of the surrounding media (1 for air), and NA is the numerical aperture of the microscope objective. The most commonly used microscope focusing element is a reflective Cassegrain objective, which is commercially available and features numerical apertures (NA) up to ~ 0.7 [58]. The above formula indicates that the lateral resolution varies along the IR spectrum from $25\text{ }\mu\text{m}$ (at 400 cm^{-1}) to $2.5\text{ }\mu\text{m}$ (at 4000 cm^{-1}). Even if the lateral resolution can be improved by a factor of four by using germanium attenuated total reflection objectives it is insufficient to reach the nanoscale range [59,60].

Using mid IR as a diagnostic tool at the hospital [35–41] or to assess more deeply the biochemical parameters responsible to the genesis of PMCD [6] led us to consider techniques able to characterize nanometer scale PMCD. For the clinician, an early characterization of a disease is a key factor to efficiently treat the patient with specific drugs [19,20].

At least two possibilities exist to perform IR spectroscopy beyond the diffraction limit i.e., to bridge the resolving power gap between the micrometer and nanometer ranges. The first one is a combination of atomic force microscopes (AFM) and IR spectroscopy (AFM-IR) [61,62]. The second one is the Optical PhotoThermal IR (OPT-IR) spectroscopy [63]. The first one has been already applied in the case of abnormal deposit of a widely prescribed antibiotic, vancomycin [64], in kidney tissue [65]. The complete set of experiments including μ FTIR as well as AFM-IR spectroscopies has given valuable information regarding the exact nature of vancomycin-associated nephrotoxicity [64–66] and of PMCD in the case of cystinosis [25].

In this contribution, we assess the advantages and limitations of OPT-IR spectroscopy for chemical investigation of PMCD in different kinds of human

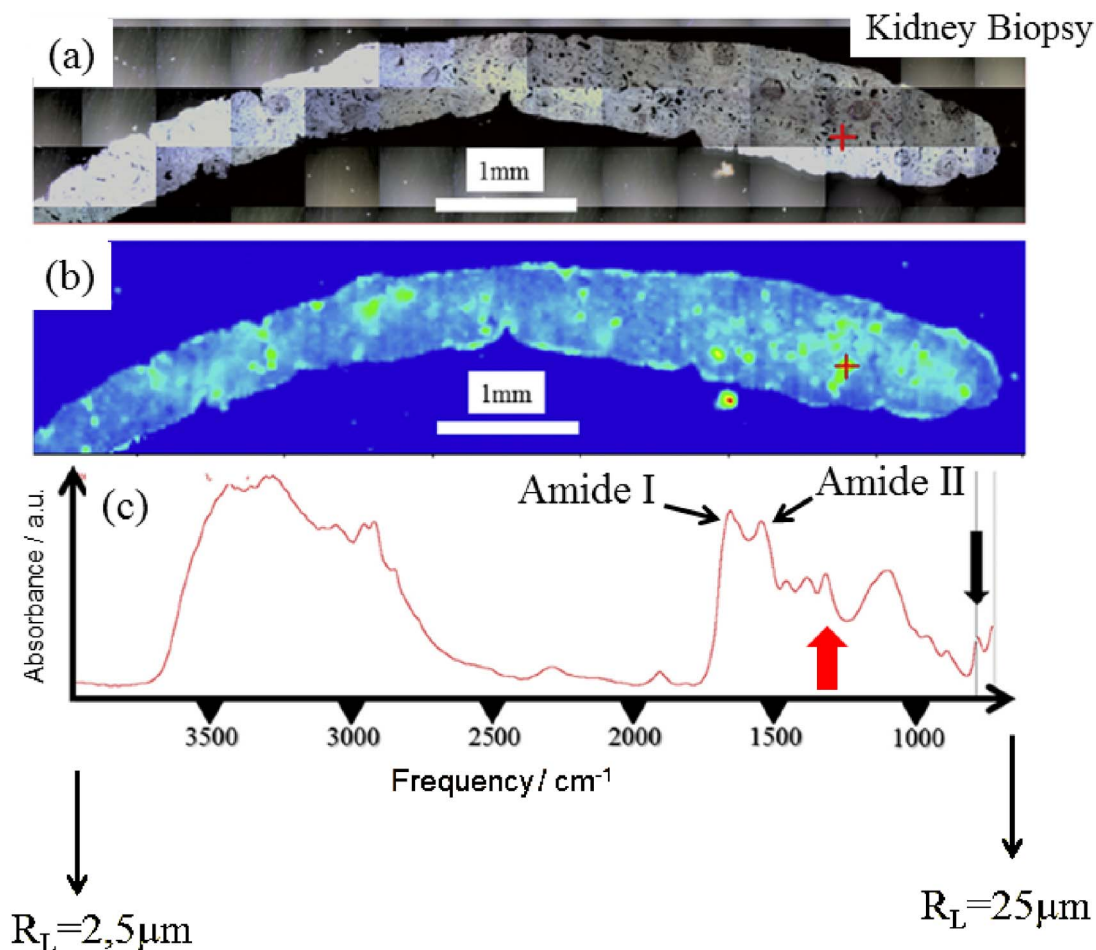


Figure 1. Biopsy from a graft kidney in a patient suffering from primary hyperoxaluria (B274). (a) Optical photography, and (b) spatial distribution of calcium oxalate monohydrate (COM) deposits in the biopsy as given by the intensity of the infrared spectrum (c) at 780 cm^{-1} . The red cross in (b) represents the biopsy point analyzed in (c) by μFTIR . We have indicated the lateral resolution (R_L) at the beginning and the end of the IR spectrum.

tissues, mostly in kidney and also in breast. In the case of kidney biopsies, we used kidney stones as reference compounds. In the case on breast biopsies, we show that other organs can be considered and that for breast tissues we assess the discrimination through OPT-IR experiments between different calcium phosphate namely amorphous carbonated calcium phosphate (ACCP), calcium phosphate apatite (CA) and whitlockite (Wk) which constitutes a key point for medical diagnostic. The ultimate goal is to evaluate if OPT-IR offers a better balance between chemical specificity and spatial resolution than μFTIR [56,57], Raman [67–69] for the iden-

tification of nanoPMCD.

2. Methods

The very first photothermal deflection experiments were published three and four decades ago [63, 70]. Basically, such an experiment is based on a pump-probe architecture using two laser sources, one for mid-infrared excitation (the pump) and the other one for measuring the photothermal effect (the probe). These two lasers are collinearly combined by a dichroic mirror. Such architecture is associated

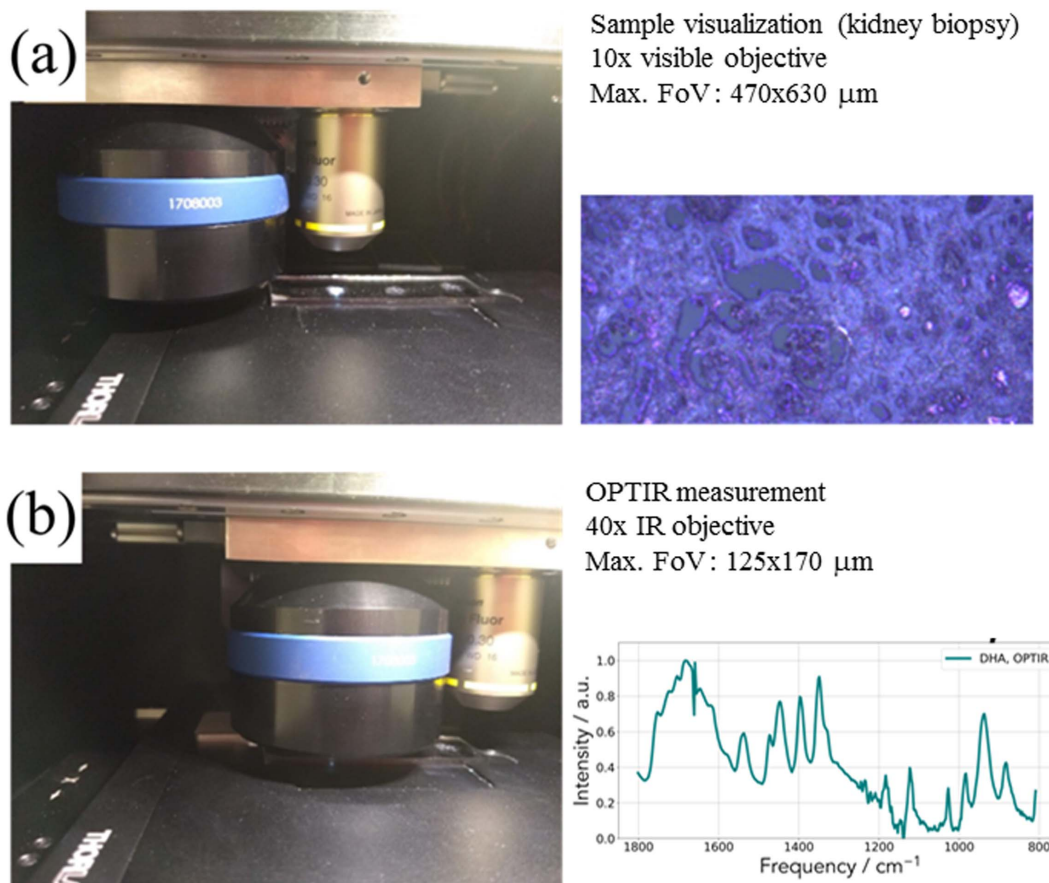


Figure 2. Experimental set up used for the characterization of pathological deposits. (a) Sample visualization with an optical microscope. (b) Schwarzschild objective for the acquisition of the IR spectrum.

with a better spatial resolution through a (visible) optical probe beam that can be focused much smaller than the IR beam. While, as previously mentioned, the lateral resolution of IR microscopy is equal to several micrometers, the lateral resolution of an OPT-IR microscope is around with 500 nm [71].

Another major advantage is that an OPT-IR microscope is a non-contact technique. It offers thus the opportunity to investigate thick samples (even several centimeters) i.e., surfaces without the contact limitations of an ATR (attenuated total reflection) device. This is of primary importance because the presence of pathological deposits in tissue constitutes a significant difficulty to obtain very thin samples. In this contribution, we have made the choice to collect OPT-IR on samples which have been previously studied by μFTIR and Field emission Scanning

Electron Microscopy coupled with energy-dispersive X-ray analysis (FE-SEM-EDX) [72]. We have already shown that the possibility to perform different experiments on the same sample led to more significant information for the clinician [54,73,74]. Note that regarding the samples, ethical approval was obtained by the ethical committee of Tenon Hospital for this study. Each sample was only named by a study number, without indication of the name of the patient or potential identification data.

In the case of our experiments (Figure 2), OPT-IR measurements (spectra and images) were acquired on the mIRage™ Infrared Microscope (Photothermal Spectroscopy Corp., Santa Barbara, CA, USA). Spectra were performed in reflection mode, 2 cm^{-1} spectral data point spacing, through a 40 \times , 0.78 NA, 8 mm working distance Schwarzschild objective. The pump

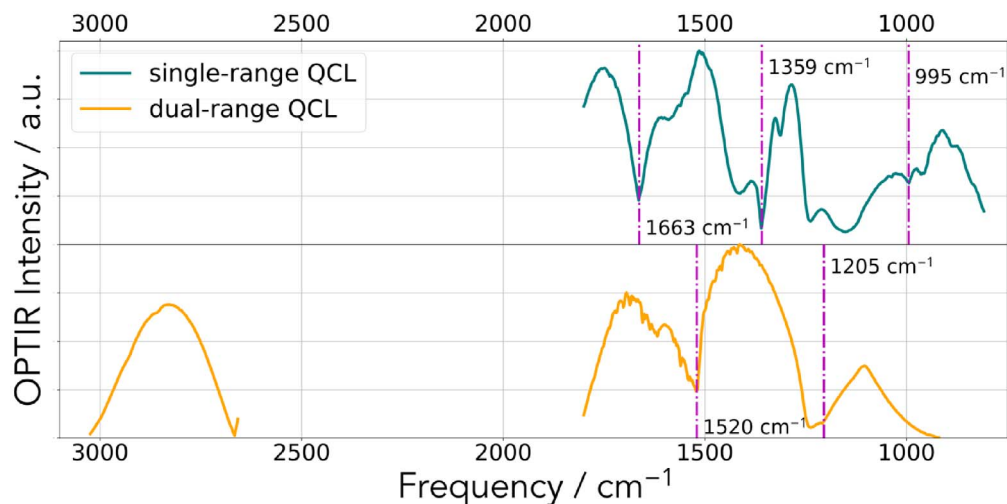


Figure 3. Typical IR spectrum corresponding of the incident beam. Dashed magenta lines show the laser stage transition frequencies.

IR sources were two pulsed, tunable four-stage Quantum Cascade Laser (QCL) devices, scanning from 800 to 1900 cm^{-1} or 920–3050 cm^{-1} (with a gap between 1800–2600 cm^{-1}). Regarding the probe, we used a CW 532 nm visible variable power laser.

Our biological samples were placed either on a CaF_2 substrate or on low- e reflective microscope slides (MirrIR, Kevley Technologies, Tienta Sciences, Indianapolis). In our case, we have not remove artifacts potentially arising due to imperfect switching between neighboring QCL laser stage (Figure 3). We used the open-source Quasar software (<https://quasar.codes>) and the Orange Spectroscopy toolbox for multivariate statistical analysis [75]. To generate data of high signal-to-noise ratio, 20–50 spectra were collected. In Figure 2, we can see a typical IR spectrum corresponding to the DHA compound. Two configurations have been used (Figure 3). In the first configuration, the transitions between the different IR sources are clearly visible and are positioned at 1663 cm^{-1} , 1359 cm^{-1} and 995 cm^{-1} . In the second configuration, the transitions between the different IR sources are clearly visible and are positioned at 1520 cm^{-1} and 1205 cm^{-1} (Figure 3).

Regarding classical FTIR spectroscopy [46,47], each kidney stone was analyzed in absorbance mode on a Bruker Vector 22 spectrometer by accumulation of 32 spectra between 4000 and 400 cm^{-1} , with resolution 4 cm^{-1} and time acquisition 1 s/spectrum. For

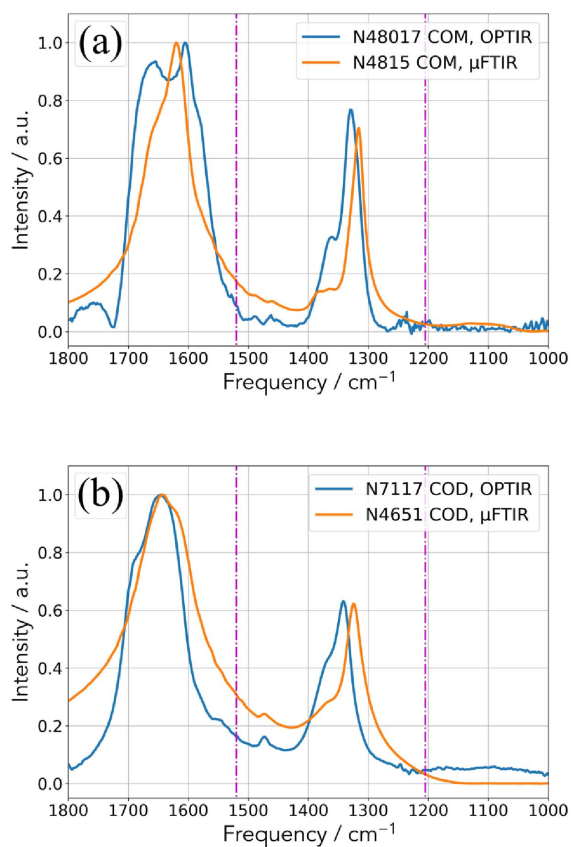


Figure 4. Comparison between the two experimental set up (OPT-IR and μ FTIR) for two COM kidney stones (N48017 and N4815) (a) and two COD kidney stones (N7117 and N4651) (b).

the biopsy, FTIR hyperspectral images were recorded with a Spectrum Spotlight 400 FTIR imaging system (Perkin Elmer Life Sciences, France).

3. Results and discussion

Thanks to the opportunity offered by a commercial experimental set up device, numerous kinds of samples have been already investigated through OPT-IR spectroscopy encompassing submicrometer atmospheric particles [76], polymers [77], fragments from a historical painting [78] or nanocomposites [79]. Several exciting research works have also been published on biological samples [80–89]. Among them we can quote the possibility to discriminate different types of lung cells on histopathology glass slides [80], to determine relevant molecular structures directly in neurons [81] as well as the orientation of collagen in tendon [82].

In all these publications, the OPT-IR technique provides an elegant non-contact way to chemically identify different kind of compounds with higher spatial resolution than conventional IR microscopes, while maintaining the advantages of an optical microscope-based platform. We would like to show different microcrystalline pathologies on which OPT-IR can bring valuable information to the clinician. To attain this goal, it is of primary importance to compare the IR spectrum acquired with a classical experimental set-up related to classical IR spectroscopy to IR spectrum collected with a OPT-IR one for different compounds namely calcium oxalate monohydrate, calcium oxalate dehydrate, calcium phosphate apatite and magnesium ammonium phosphate hexahydrate.

3.1. Biological reference compounds collected at the nanometer scale

In Figures 4 and 5, we have selected a set of reference compounds corresponding to different chemical phases identified in kidney stones and compared their IR spectra obtained with two experimental set up, namely μ FTIR and OPT-IR configurations. In figure 5, we can see that some differences exist between μ FTIR and OPT-IR for calcium oxalate monohydrate (COM) [89–91] (Figure 4a) and dihydrate (Figure 4b) [92] mainly due to the transition between

the laser stages. In both cases, around 1200 cm^{-1} , the incident IR signals by the mIRage™ experimental set up are quite noisy in line with weak intensity of the IR laser in this part of the spectra.

Regarding calcium oxalate monohydrate (Figure 4a), the assignment of the most intense IR bands (1618 cm^{-1} , 1312 cm^{-1} , 782 cm^{-1} , 667 cm^{-1} , 514 cm^{-1}) is well known [89–91]. More precisely, high absorbance at 1618 and 1312 cm^{-1} belong to C=O and C–O, respectively. Regarding calcium oxalate dehydrated (COD) (Figure 4b), the most intense vibrations are shifted at 1643 cm^{-1} and 1325 cm^{-1} [91,92].

Regarding the phosphate salts (Figure 5), we have considered two biological reference compounds: calcium phosphate apatite (CA) [93–96] and struvite (magnesium ammonium phosphate hexahydrate, MAP) [16,18].

Clearly, some differences exist which may have different origins. The first one is related to the fact that μ FTIR gives an average chemical composition (the quantity sample is around μg) while OPT-IR gives a local chemical composition (the size of the probe spot is 500 nm). Actually, biological samples have never made of only one component and always they contain at least some proportions of matrix compounds such as proteins. In addition, kidney stones are made of two or more crystalline species in more than 93% of cases. It is thus possible to collect an IR spectrum dominated by proteins with the OPT-IR experimental setup with a sample for which the chemical composition given by μ FTIR is 99% COM and 1% proteins. Finally, the presence of amorphous calcium phosphate which is associated to a shoulder in the absorption band positioned at 1030 cm^{-1} FTIR spectra has to be considered.

Moreover, a chemical analysis based on IR lasers at the nanometer scale still constitutes a challenge. For example, Mathurin *et al.* [97] shows experimental data which reveal significant differences in the agreement between AFM-IR and conventional FTIR data, depending on the studied mineral. More precisely, the spectra recorded in AFM-IR and FTIR microscopy are very similar in the case of the smectite (Figure 6a). But if they consider AFM-IR and FTIR spectra collected for forsterite single crystal, some band positions as well as some band ratios are drastically different (Figure 6b).

The origin of such huge spectral differences observed in the case of the forsterite crystal is multi-

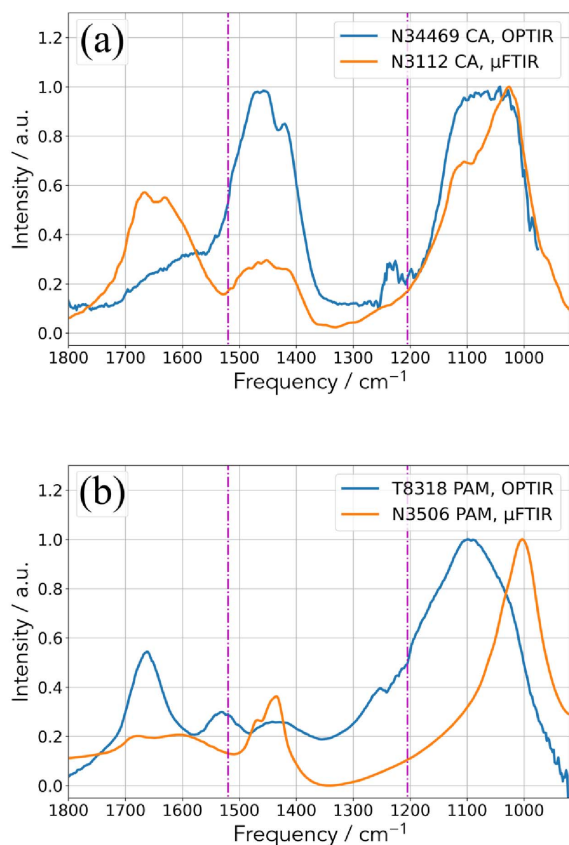


Figure 5. Comparison between the two experimental set up (OPT-IR and μ FTIR) for (a) two CA kidney stones and (b) two MAP kidney stones.

ple. Crystal orientation, the optical behavior of the sample as well as geometry of the experiments may have significant effects on the IR spectrum. Also, scattering processes of laser with wavelengths close to the dimensions of the crystals may have to be considered.

3.2. Hyperoxaluria and calcium oxalate monohydrate ectopic calcifications

As noticed recently by Aleigh and Petros [98], despite considerable improvements in the development of new therapies, the incidence of urolithiasis increases worldwide affecting 12% of the world population at some stage in their lifetime. Calcium-based stones are predominant renal stones comprising about 80%

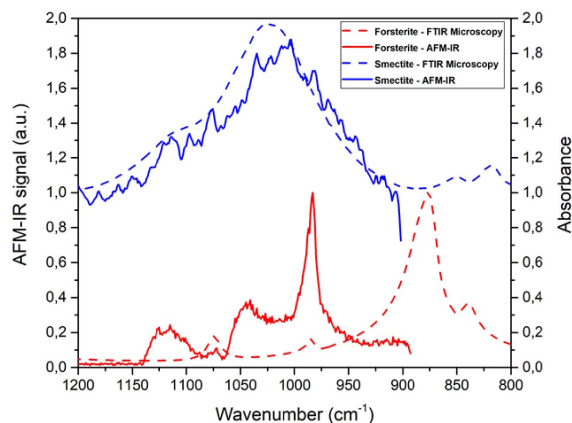


Figure 6. Comparison of the FTIR microscopy spectrum (dashed line) and the AFM-IR spectrum (line) obtained on smectite powder (blue) and on forsterite polished sections (red). Both AFM-IR spectra are obtained in contact mode with top-down illumination and gold coated tip.

of all urinary calculi [99]. Such high prevalence explains the fact that several studies have been dedicated to the crystallography and the chemistry of calcium oxalate compounds [100–104].

Crystalline calcium oxalate exists in three hydrated forms known as monoclinic whewellite (monohydrate, COM) [89,91], tetragonal weddellite (dihydrate, COD), [91,105,106] and triclinic caoxite (trihydrate, COT) [91]. Recently, amorphous calcium oxalate has been synthesized [107,108]. This compound constitutes a transition step during the chemical transition between COD and COM, the last one being the more stable [109,110]. Regarding their prevalence, COM is the most frequent, while COD is about two to three times less common [111]. The trihydrate form is rarely observed [112]. Another significant clinical difference between COM and COD comes from the fact that in clinical practice COM is related to hyperoxaluria states while COD is associated to hypercalciuria ones [113,114].

Regarding the presence of ectopic calcification made of calcium oxalate, as usual [4,49,115], we start by observations through a FE-SEM-EDX microscope (Figures 7a–c). In this contribution, we have used a Zeiss SUPRA 55VP FE-SEM. To preserve the structural and the chemical integrities, All the SEM observations are made at low voltage (1.4 keV) and with-

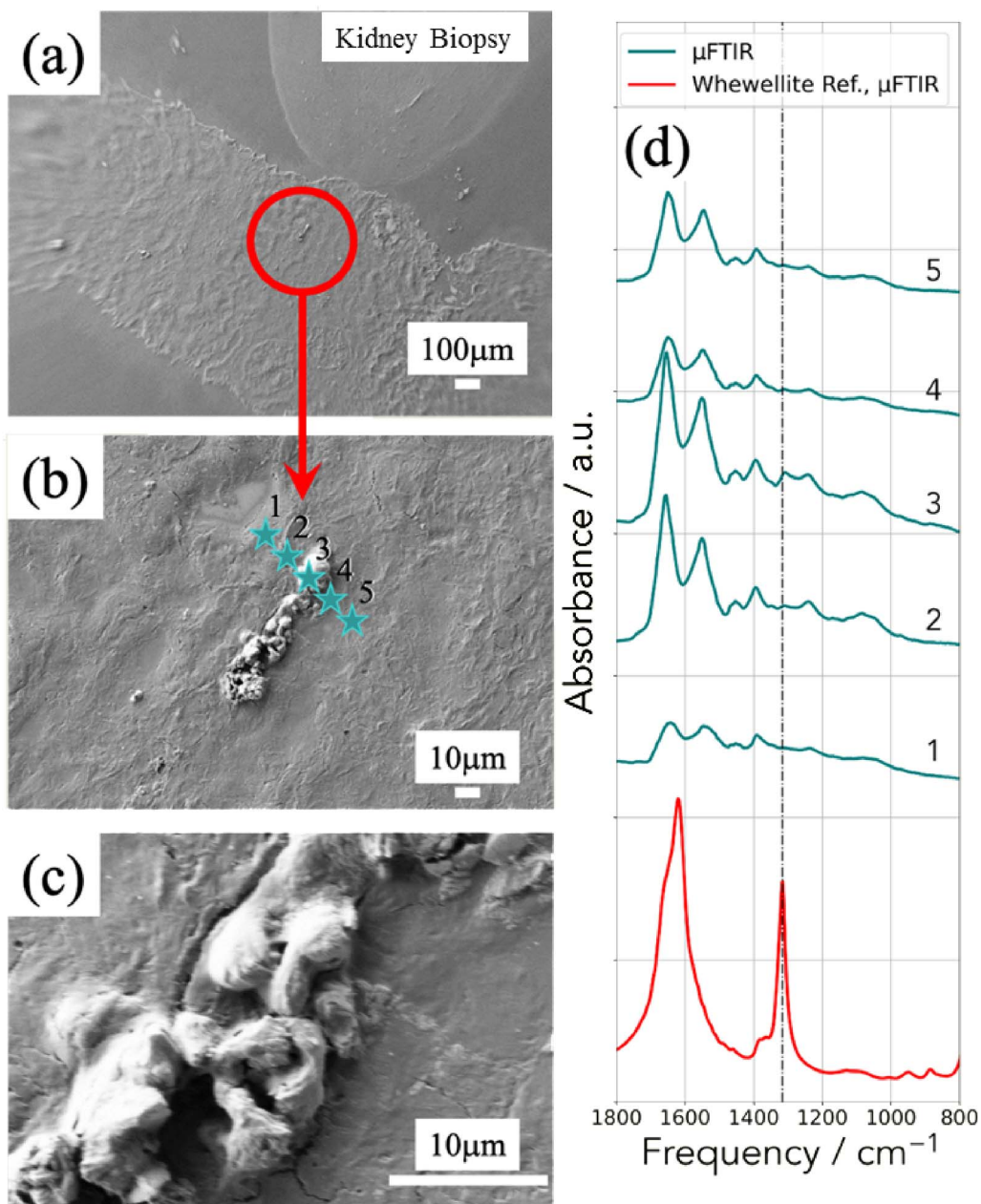


Figure 7. (a–c) Scanning electron microscopy at different magnifications of ectopic calcification present in a kidney biopsy. (d) FTIR spectra collected for the different locations of the IR beam as indicated in (b).

out the usual deposits of carbon at the surface of the sample. Such observations allow us to localize precisely the PMCD in the kidney biopsy. In Figure 7d, we can see IR spectra collected on different points of interest (POI) defined in Figure 8b.

As discussed previously, due to the micrometer

spatial resolution of the FTIR spectrometer, we can observe the two bands amide I and II associated to the tissue even if the probe is positioned on the calcification (location 3 in Figure 8b). As it is generally the case, their relative intensities are not always the same. This is due to the preparation proto-

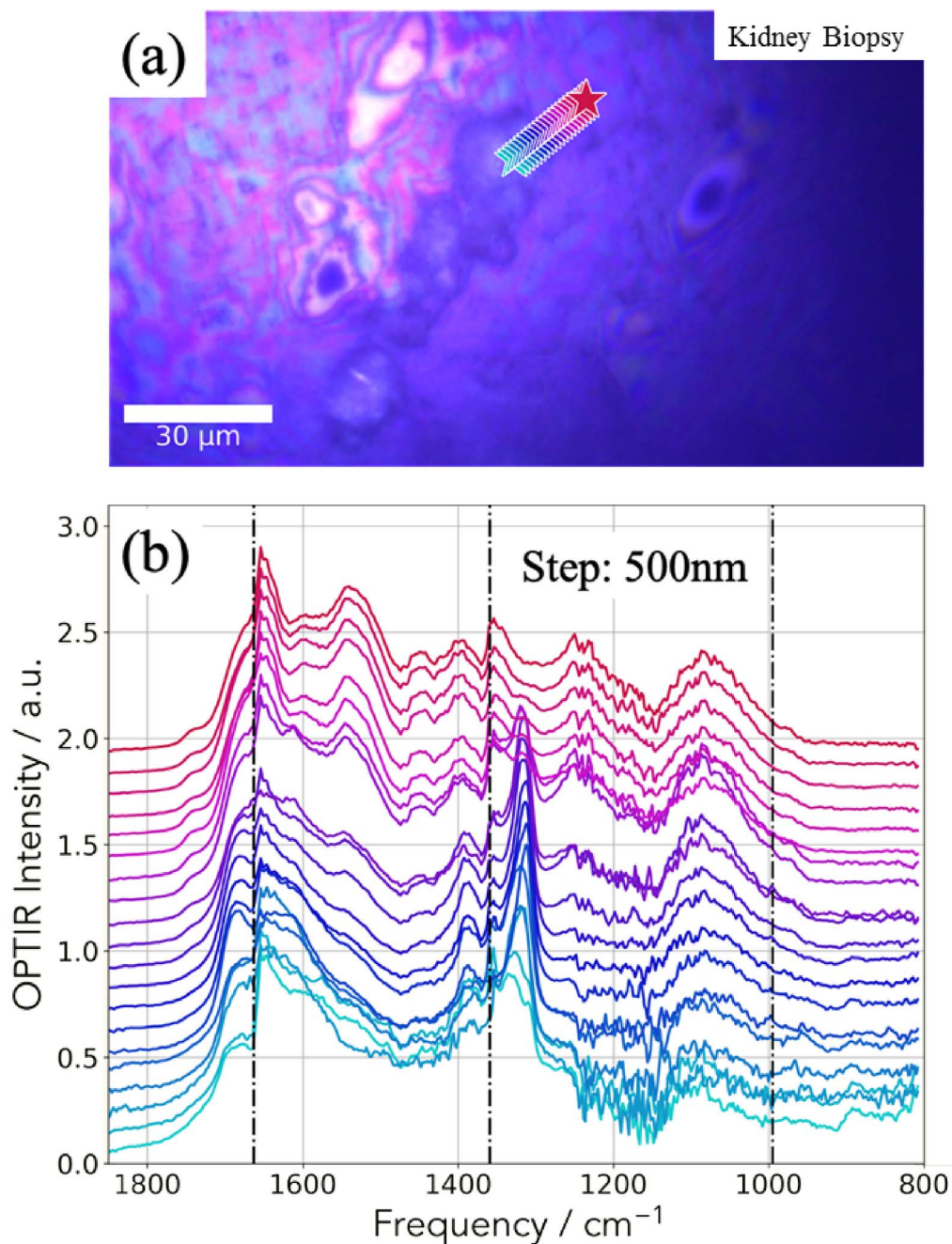


Figure 8. (a) Optical image collected by the OPT-IR microscope. (b) 20 OPT-IR spectra collected along the line defined in (a).

col which is optimized to preserve the physicochemical integrity of the ectopic calcification. Regarding the chemical composition of the ectopic calcifications, the presence of IR bands at 1315 cm^{-1} clearly indicates the presence of calcium oxalate monohy-

drate (its spectrum has been plotted at the bottom of Figure 7d).

The IR spectra collected by the mIRage™ experimental set up are presented in Figure 8b, each spectrum corresponding to a star shown in Figure 8a.

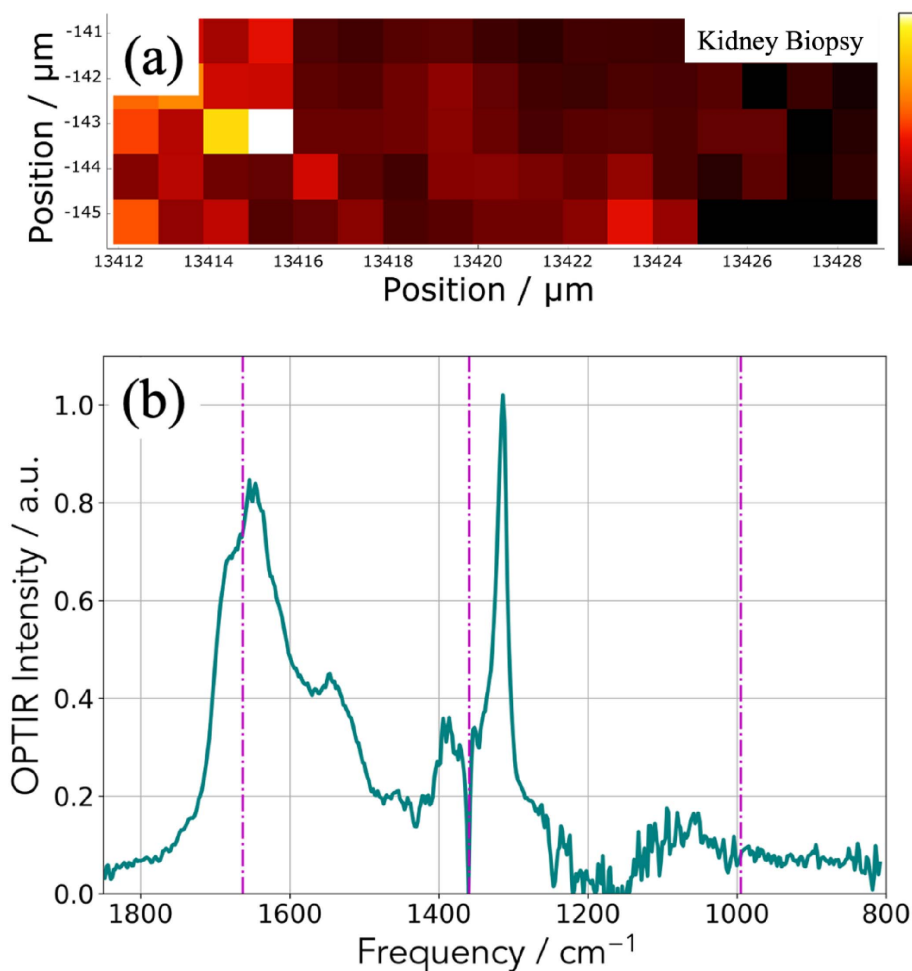


Figure 9. (a) Spatial distribution of the integrated 1302–1327 cm^{-1} IR absorption band specific to COM. (b) OPT-IR spectrum from the highest intensity (white) pixel of (a). Spectra were smoothed with a 5-point Savitzky–Golay filter and normalized to the integral between 1600–1850 cm^{-1} .

As we have observed through μFTIR spectroscopy, the relative intensity between the amide I and II are not the usual ones. An additional explanation of this observation comes from the transition between the two IR laser stages which is positioned on the amide I band. For this sample, thanks to the high spatial resolution, we have collected an IR spectrum every 500 nm (Figure 8b). The observation of a sudden modification of IR spectra when the probe move on the ectopic calcification indicates that the spatial resolution of the mIRage experimental set up is effectively around 500 nm. Note that the intensity ratio of the two bands of COM (1315 and 1618 cm^{-1}) may

be not always the same due to the fact the two lasers used here are polarized. Also note the variation of the position of the band at 1315 cm^{-1} which may be due to the same reason.

In Figure 9, another way to collect IR data is shown. We select an absorption band of the OPT-IR spectrum (Figure 9b) which corresponds here for calcium oxalate monohydrate (Figure 8a) and we have plotted the maximum of this absorption band versus its position to obtain the spatial repartition of COM with a lateral resolution of 500 nm (Figure 9a).

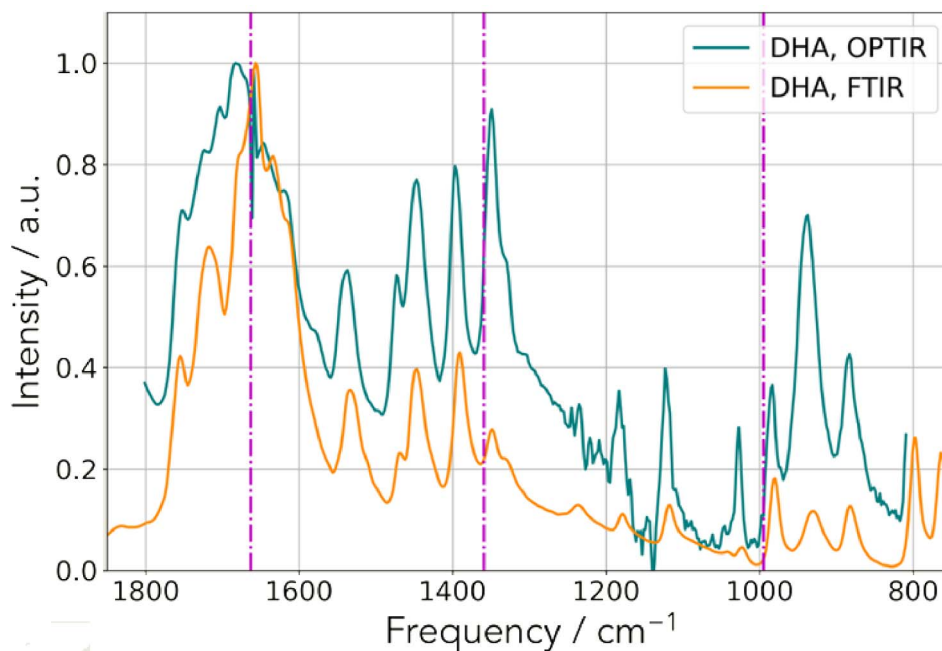


Figure 10. Comparison between techniques. IR spectrum collected on a classical FTIR device (orange) and an OPT-IR spectrum acquired on the mIRage™ experimental set up (teal).

3.3. The adenine phosphoribosyltransferase (APRT) deficiency

Among the genetic diseases which induce the formation of ectopic mineralizations in kidney we can quote adenine phosphoribosyltransferase (APRT) deficiency which is a rare autosomal recessive disorder. This genetic disease induces the formation of 2,8-dihydroxyadenine (DHA) stones and renal failure secondary to intratubular crystalline precipitation [24,116,117]. Different ways exist to establish the medical diagnosis including the identification of typical DHA crystals in urine or renal biopsy, a genetic investigation as well as the measurement of APRT activity in erythrocytes. As underlined by Bollée *et al.* [117], early diagnosis of the disease is critical because patients may develop renal failure [118–120] that may be efficiently prevented by allopurinol, a xanthine oxydase inhibitor. We have already demonstrated that μ FTIR spectroscopy constitutes an elegant way to perform an early diagnosis of this genetic disease [121].

We performed IR experiments using an OPT-IR experimental set up. For that purpose, we start by considering a kidney stone made of DHA and by collect-

ing IR spectra. As we can see in Figure 10, the spectral correspondence and excellent signal to noise ratio allows the clinician to recognize the IR spectrum of DHA crystals [24,55,121].

After obtaining these results, we inspected a mouse (as an animal model for this pathology) as well as a human biopsy. Regarding the human biopsy, SEM observations allowed us to localize abnormal deposits (Figure 11). μ FTIR spectra were collected (Figure 12) clearly show the presence of DHA crystals.

On this human biopsy, mIRage experiments have been also performed and we can see in Figure 12, these IR spectra clearly underline the presence of DHA crystals. One interesting point is that the amide I and II bands are not always visible. It seems that with a probe of 500 nm IR spectra on DHA crystals alone can be collected. As for the previous sample, it is possible to build the spatial distribution of DHA crystals from one selected IR band through its intensity (Figure 13).

Figure 14 shows the potential of OPT-IR in hyperspectral measurements through an example of hierarchical cluster analysis. Here, we have calculated the Euclidean distances of individual spectra and used

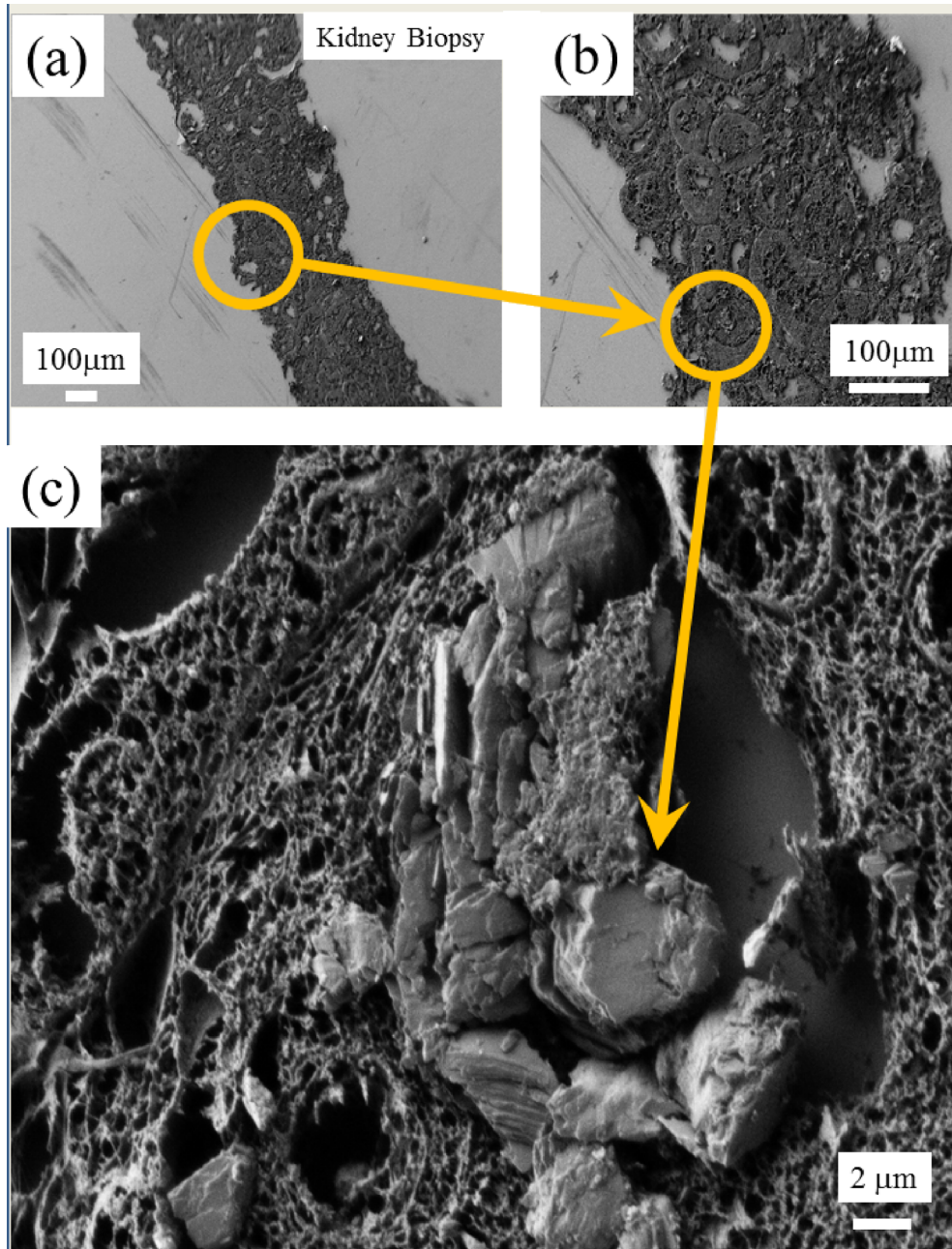


Figure 11. SEM images of DHA deposit at different magnifications present in a human kidney biopsy.

the Ward linkage to determine cluster distances. Plotting the spatial distribution of the Euclidean distance of each spectrum from the average spectrum (Figure 14a) highlights a high-intensity area in the middle of the map. The result of HCA is shown in Figure 14b, where the top two clusters are highlighted

in red and blue. By calculating the cluster averages for each cluster, we can clearly identify the DHA rich area different from the average spectrum of the surrounding tissue (Figure 14c).

Regarding the mouse kidney, we used the 500 nm probe to underline the possible presence of DHA

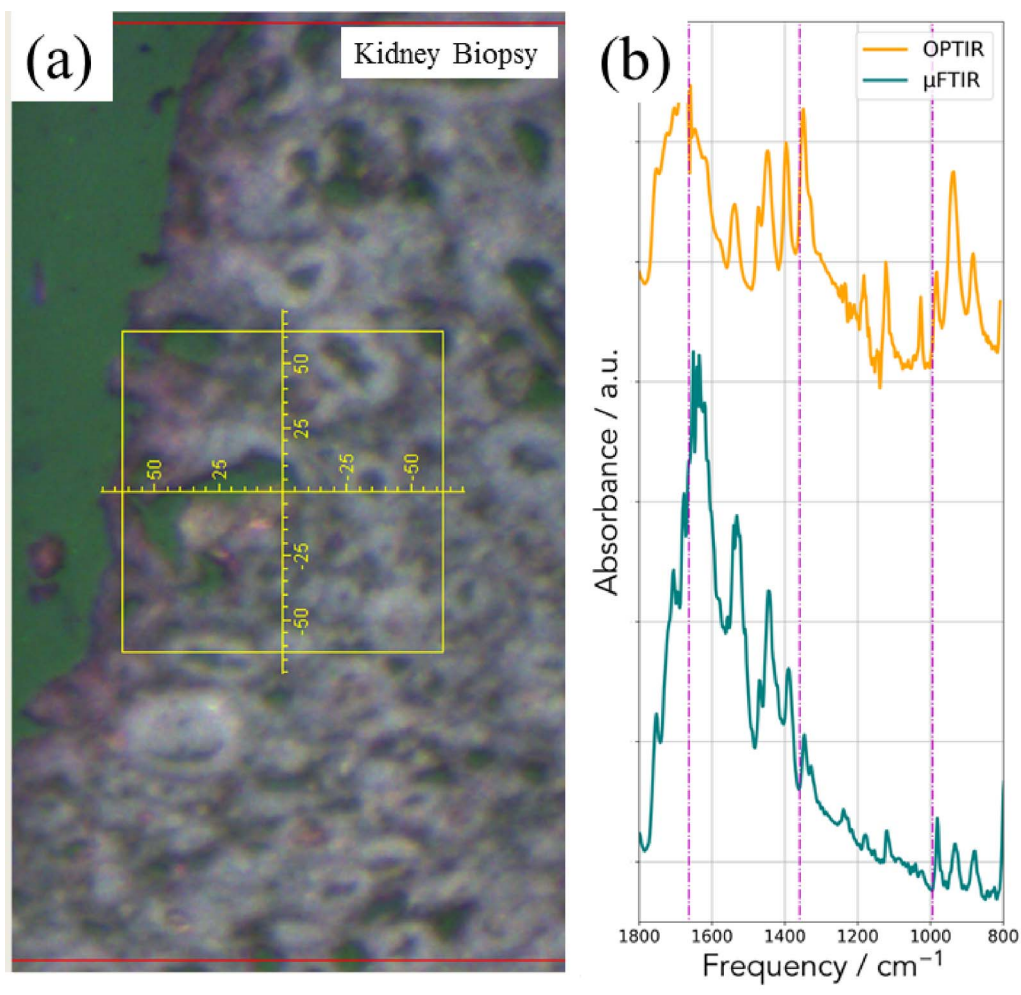


Figure 12. (a) Optical photograph. (b) IR spectra (with the μ FTIR and the OPT-IR experimental set up) showing the presence of DHA crystals.

crystals. In Figure 15a, we selected two areas of interest (Figures 15b and c). For each area, we collected IR spectra using the mIRageTM experimental set up (Figures 16 and 17). One simple way to analyze the IR data can be performed by considering the 1000–800 cm^{-1} region where DHA has quite intense IR absorption bands.

The different IR spectra collected with the mIRageTM experimental set up show significant differences with the IR spectra corresponding to DHA. Thus, DHA seems to be absent (Figures 16 and 17).

3.4. Giving major information through nondestructive techniques

With the help of OPT-IR nanospectroscopy and SEM-EDX, it is possible to gather information regarding the chemistry and the topology of kidney stones without any kind of preparation. In a recent paper, we have also combined micro computed tomographic imaging (micro CT) and SEM-EDX [122]. Micro CT is a powerful tool for visualizing urinary stones allowing easy visualization of stone structure and mineral identification, especially if an attenuation standard is included with a specimen [122–126]. Regarding micro CT, experiments were conducted using the

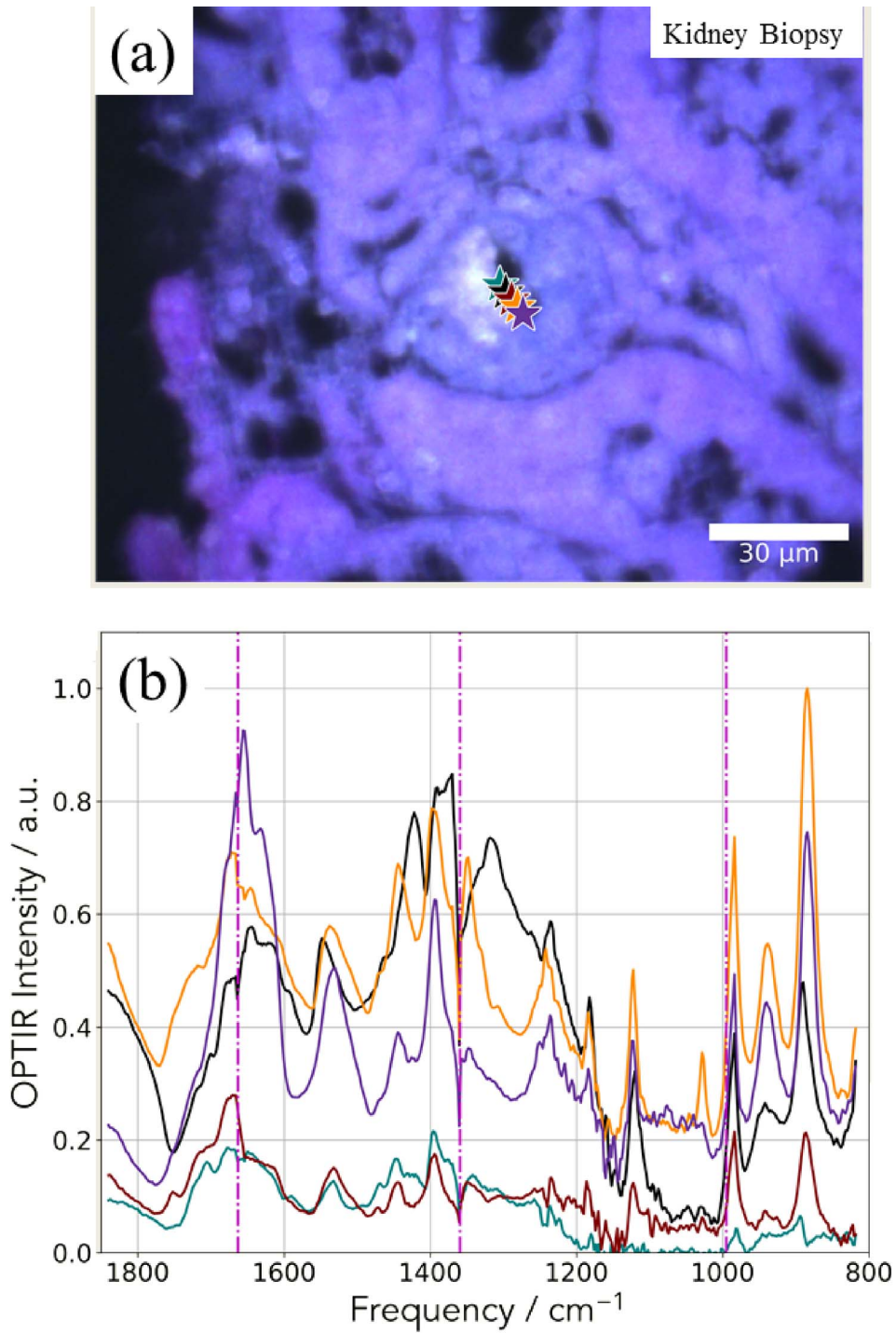


Figure 13. (a) Optical image; (b) OPT-IR spectra showing the presence of DHA deposits in a human kidney biopsy.

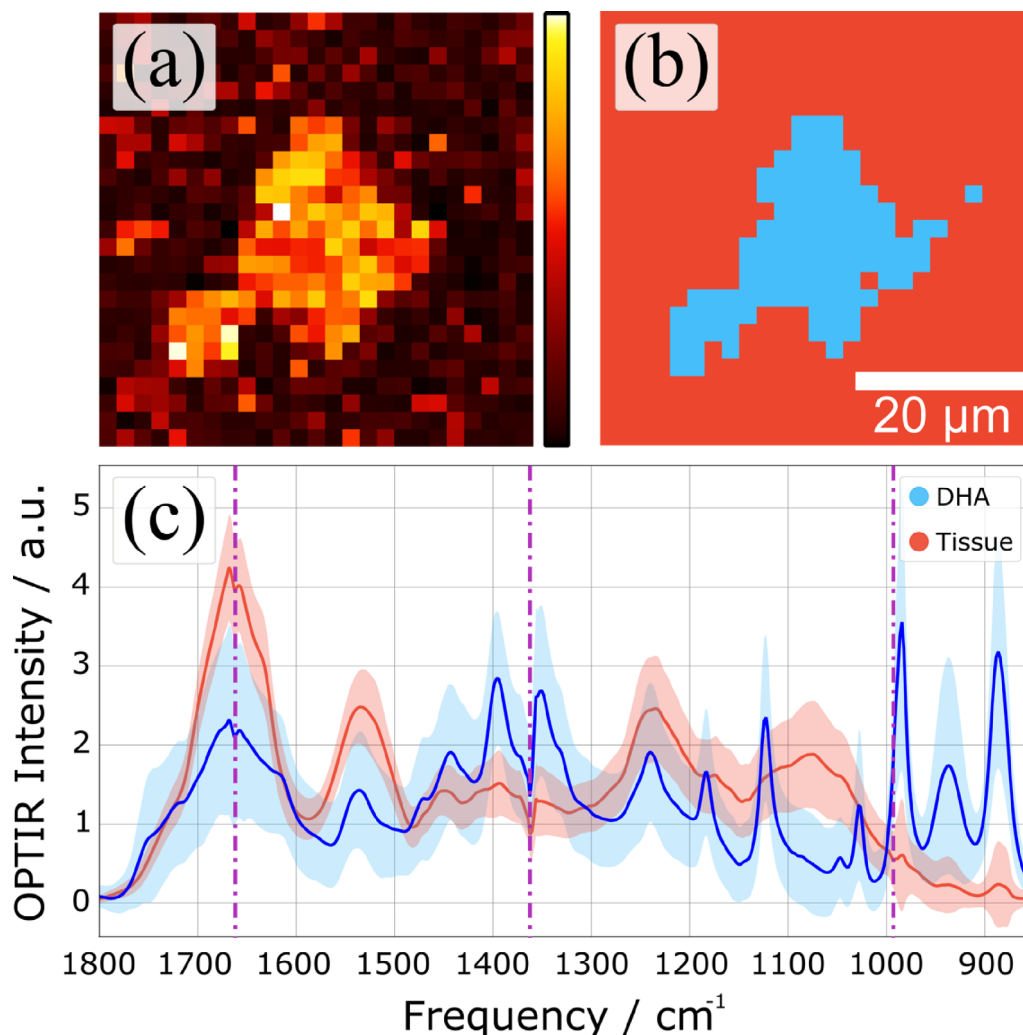


Figure 14. Hierarchical cluster analysis (HCA) of a hyperspectral dataset. (a) Spatial distribution of the Euclidean distance from the average spectrum. (b) Spatial distribution of two clusters identified by HCA. (c) Cluster averages and their standard deviation.

Skyscan 1172 Micro CT system (Bruker, Kontich, Belgium), typically using 60 kVp, 0.5 mm Al filter, and 0.7° rotation step for final (cubic) voxel sizes of 2–12 μm. Stones were typically mounted in Styrofoam for scanning, as that material is remarkably X-ray lucent [122].

We have considered here two kidney stones. The first one was collected as part of an ongoing study of kidney stones, in which patients are consented for study under the Indiana University Internal Review Board (under guidelines from the United States Health and Human Services Office of Human Subjects protection). That stone was mainly composed

of COD. The second one comes from Tenon Hospital. It was mainly composed of COM. These two kidney stones are made of calcium oxalate, and, at their surface, a white deposit exists named Randall's plaque [127–132]. The formation mechanism of Randall's plaque, which remains incompletely understood, has been addressed in many publications during the last two decades [133–143]. As underlined by Van de Perre *et al.* [143], optical microscopy of eliminated kidney stones grown on Randall's plaque typically reveals a papillary umbilication, the imprint of the previous papillary attachment, which can be found as an irregular depression, while some stones

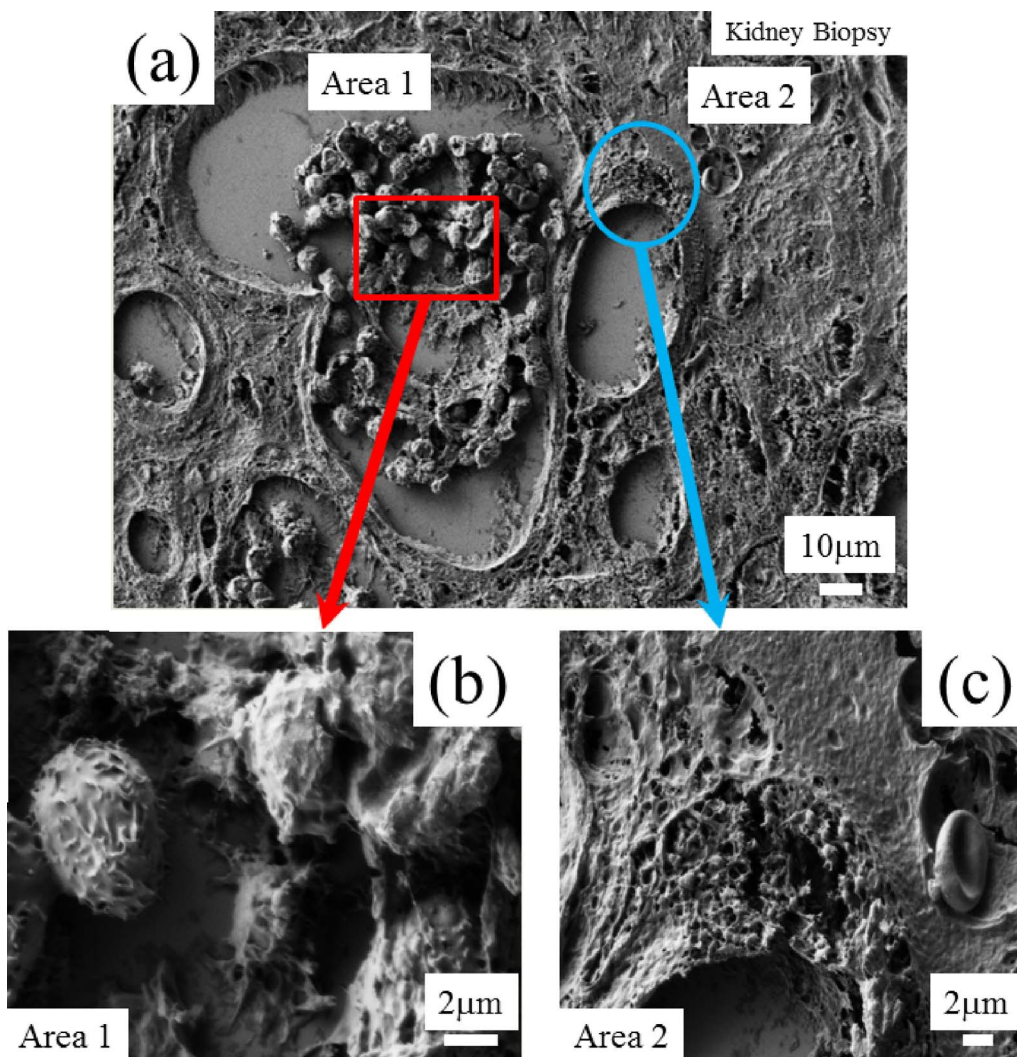


Figure 15. Scanning electron microscopy at different magnifications to select areas of interest for the mouse kidney (b) and (c).

can display plaque remnants at the umbilication as well.

In Figure 18, we can see images of the two kidney stones corresponding to SEM (Figures 18a and b) observations and micro CT (Figure 18c) for the first one (KRP 453) and SEM (Figures 18d and e) observations for the second one (86396). On SEM as well as on the micro CT scans we can see clearly the two chemical phases of the kidney stones i.e. calcium oxalate crystals and calcium phosphate apatite of the RP. The chemical analysis as given by OPT-IR spectroscopy performed for the two samples shows clearly that the

Randall's plaque was made of calcium phosphate apatite (Figure 19), a result in line with previous publications [133–144].

4. Another pathological calcifications: the case of breast cancer

As underlined previously, microcrystalline pathologies affect all the Human organs and among them the presence of calcifications in breast is of primary importance due to its possible link to cancer. Breast cancer is a worldwide public health problem and

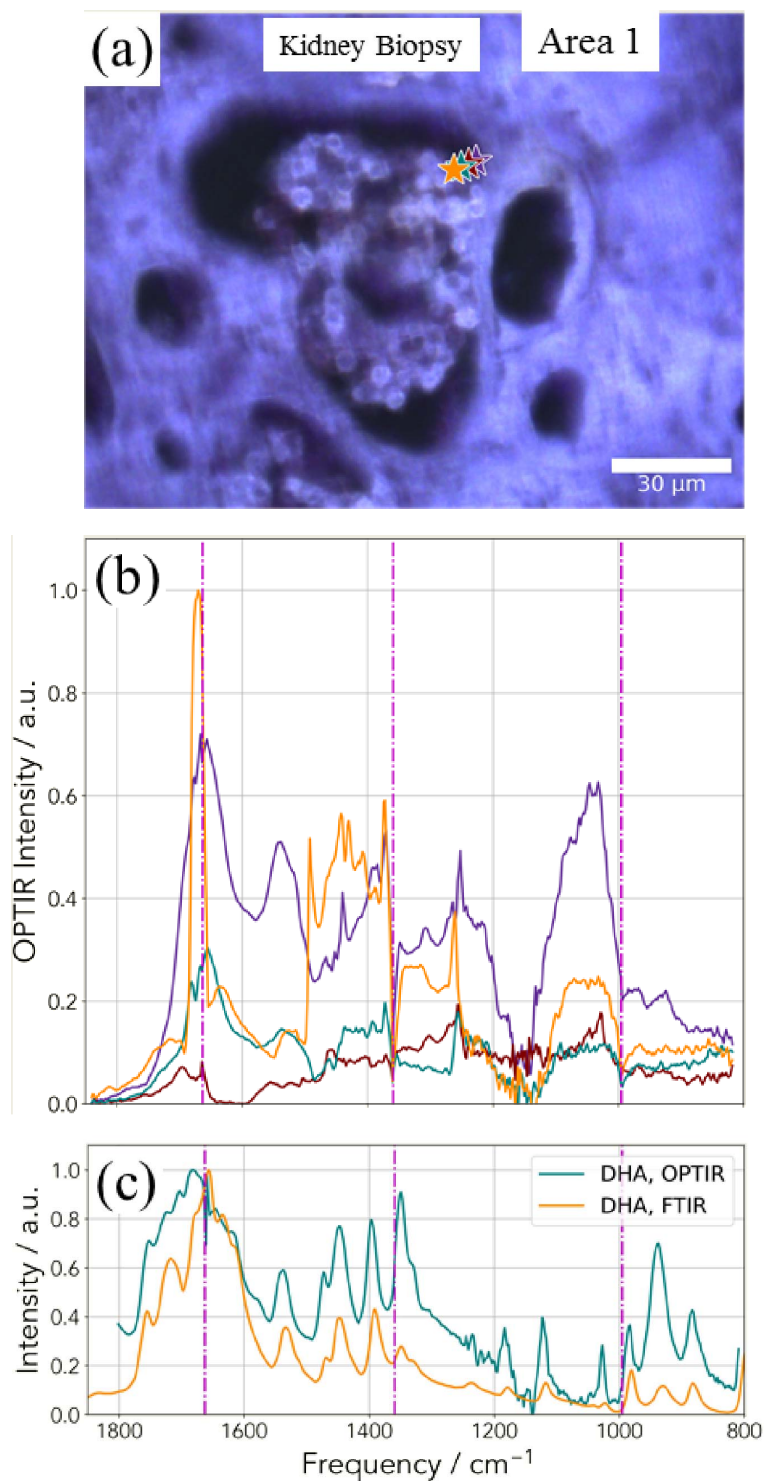


Figure 16. (a) Optical image corresponding to the deposit identified through SEM (Figure 15) and (b) OPT-IR spectra corresponding to the different points of interest (stars in a). (c) OPT-IR and FTIR spectra of DHA reference compound.

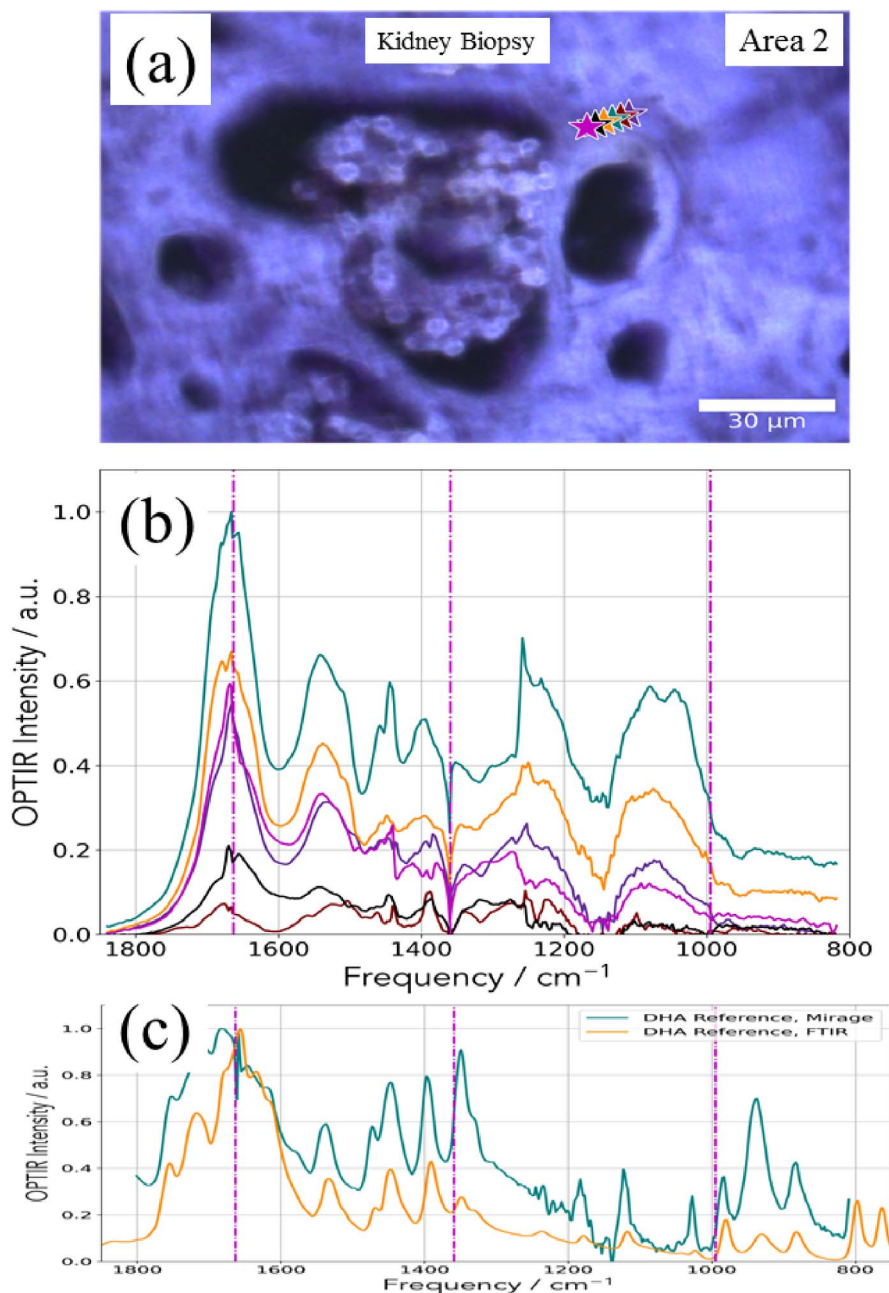


Figure 17. (a) Optical image corresponding to the deposit identified through SEM (Figure 15) and (b) OPT-IR spectra corresponding to the different points of interest (stars in a). (c) OPT-IR and FTIR spectra of DHA reference compound.

is the most common cause of cancer deaths, accounting for approximately 16% of cancer deaths in adult women [145]. Breast microcalcifications (BMC) which appear as white spots or flecks on a mammogram are related to calcifications in which the di-

ameter is less than 1 mm [146–152]. At this point, it is worth to mention that the current spatial resolution mammographs without magnification ranged between 100 and 200 μm [149].

In a recent publication, we have underlined that

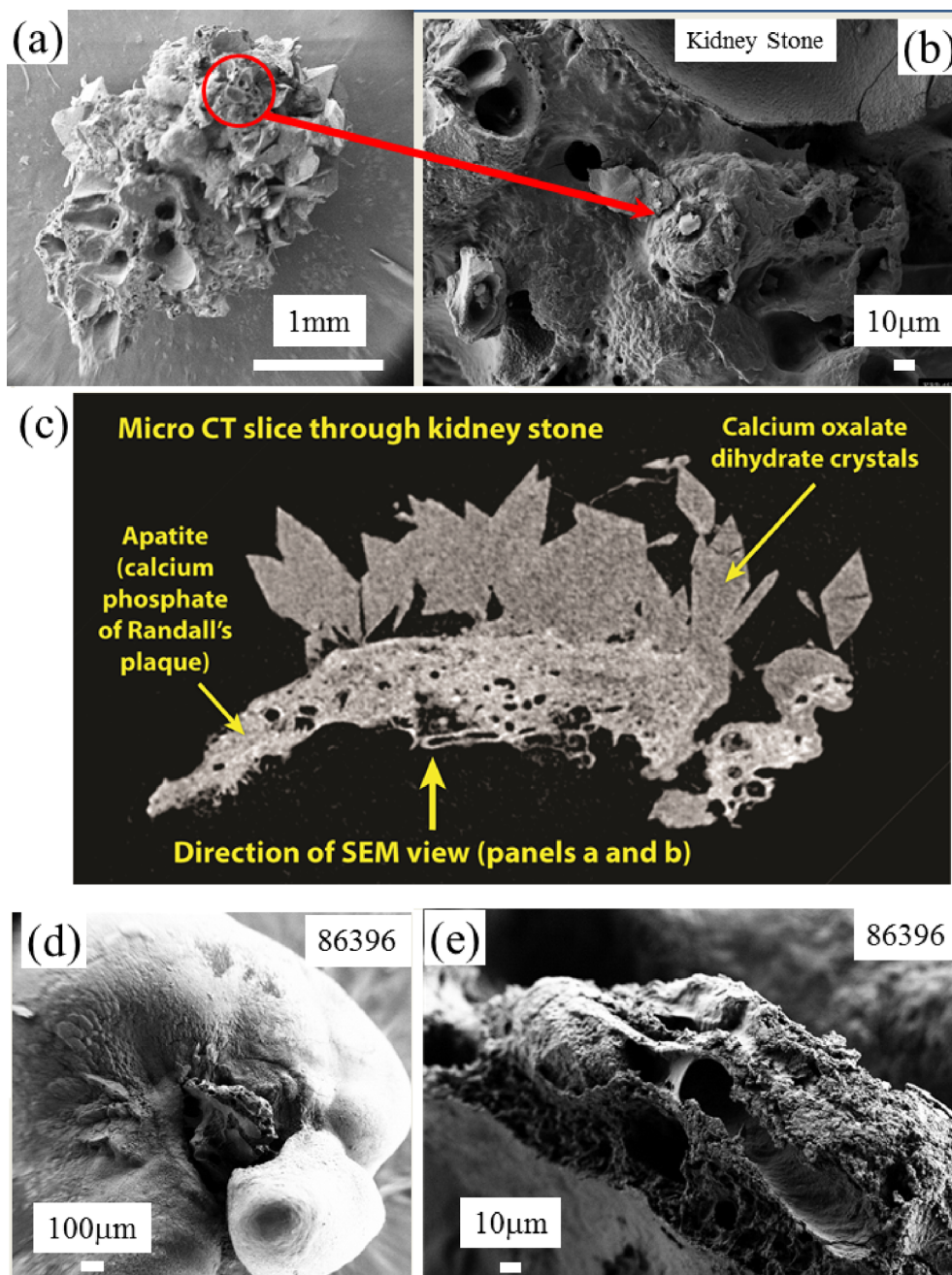


Figure 18. (a,b) SEM images of a RP at the top of a kidney stone. (c) CT tomography of the KRP 453 stone. (d,e) SEM images of a RP at the top of the kidney stone 86396.

microcalcifications as seen through usual mammography are made of nanometer scale breast calcifications made of spherical entities [8]. Such structural characteristic leads to the fact that the determina-

tion of the chemical composition of such nanometer scale entities cannot be performed through classical μ FTIR spectroscopy. This is due to the chemical diversity of BMC in which different chemical phases

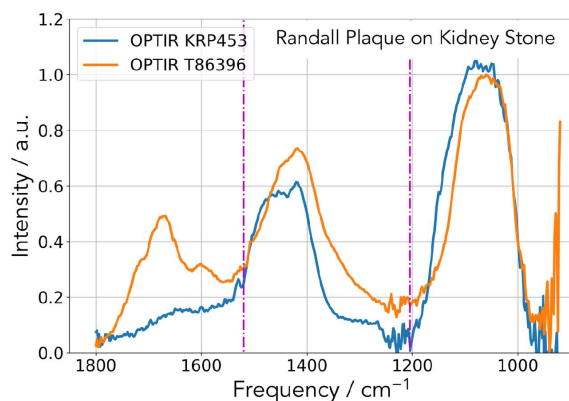


Figure 19. OPT-IR spectrum of the RP for the two samples giving the same chemical composition namely a mixing of ACCP and CA compounds.

namely calcium oxalate dihydrate [153], amorphous and nanometer scale crystals of calcium phosphate apatite with different levels of carbonatation [8,154–157] as well as whitlockite (Wk) [158–161] have been identified. For BMC, the number of chemical phases is thus quite low compared to the number of chemical phases identified in ectopic calcifications present in kidney (four instead of 24) [4,55]. It is also worth to underline the importance of micro and nano spectroscopies which are able to point out the variation of the level of carbonatation from the core to the surface of a BMC [8].

In Figure 20, we show SEM observations of micro-calcification displaying a typical morphology related to Wk (different from the one observed in kidney stones [19]). Due to the small size of this abnormal deposit, it is quite difficult to obtain an IR spectrum with a sufficient signal to noise ratio with a classical μ FTIR experimental device.

In Figure 21, we can see clearly that the OPT-IR nanospectroscopy is able to collect a significant IR spectrum which underlines the presence of whitlockite in the chemical composition of this abnormal deposit present in breast biopsy. OPT-IR nanospectroscopy seems to underline the presence of a calcium phosphate compound but it is quite difficult to say that this signal corresponds to Wk.

On Figure 22, the FTIR spectra of calcium phosphate identified in PMCD have been plotted. As we can see, it is details on the absorption bands (shoulders and shift) which are the keys to distinguish be-

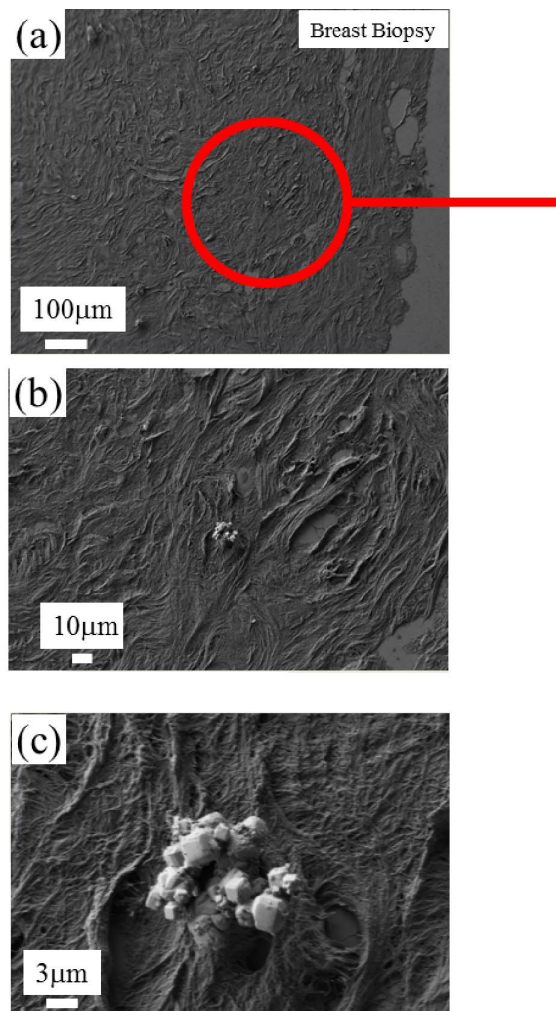


Figure 20. SEM images of an agglomeration of Wk crystals present in a breast biopsy.

tween Wk, ACCP and CA. Considering all the IR spectra we have collected through OPT-IR, it seems that such discrimination between all the calcium phosphate compounds is quite difficult.

5. Conclusion

It is well accepted in the medical community that conventional IR spectroscopy constitutes the golden standard to obtain a precise chemical composition of kidney stones. The emergence of IR spectroscopy associated to spatial resolution below one micrometer constitutes an incredible opportunity to describe

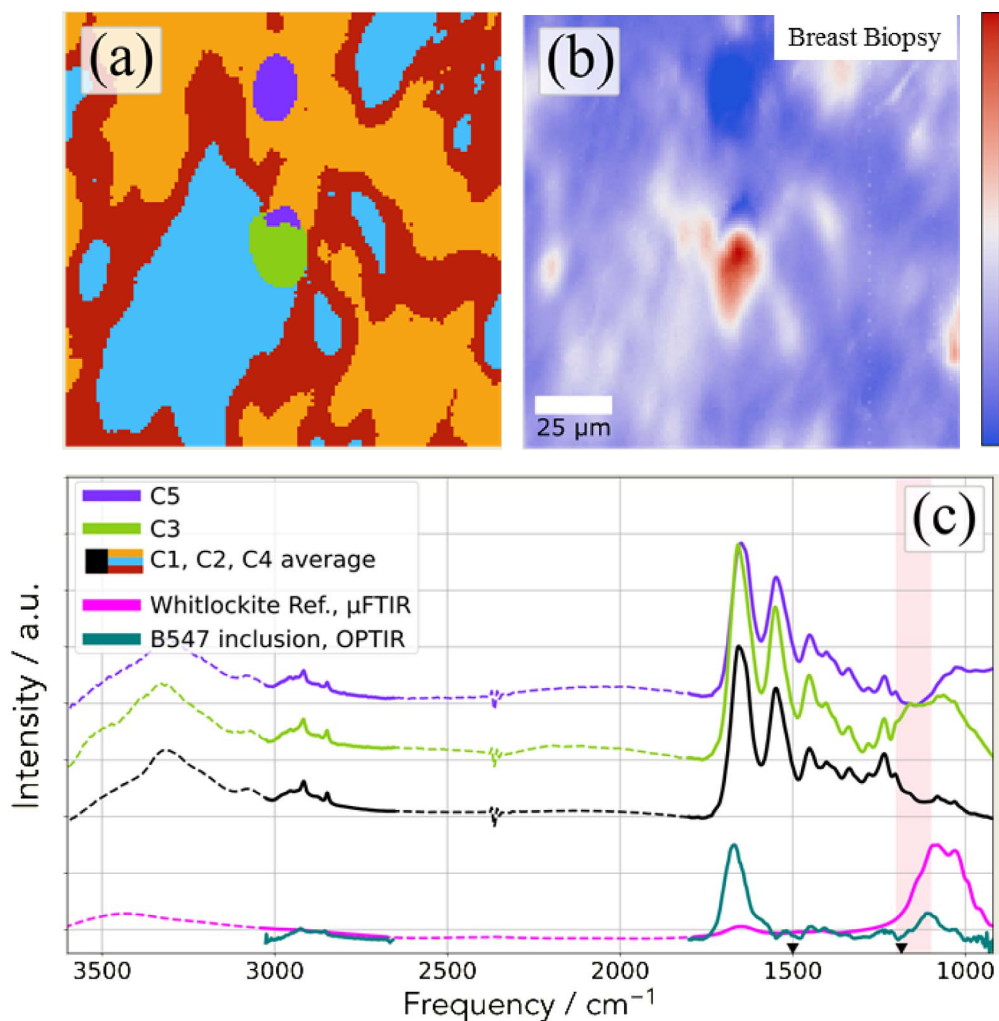


Figure 21. FTIR imaging of the deposit identified through SEM (Figure 20). (a) k-means cluster map of the observed area, the colors are related to the cluster defined on (c). (b) Distribution of the integral value between $1100\text{--}1200\text{ cm}^{-1}$ highlighted in red in the bottom panel (c) Cluster averages based on (a). Here C1, C2, and C4 clusters were merged (shown in black) as they belong to the surrounding tissue. Data were collected with an Agilent imaging set up. An OPT-IR spectrum collected from the sample inclusion of B547 and μ FTIR spectra recorded on a reference sample are shown in teal and magenta colors, respectively. The regions accessible with the dual-band QCL are plotted with continuous and the parts not covered by the laser with dashed line.

chemical heterogeneity or interface of complex biological samples.

In this contribution we have considered different chemical phases which have been identified in pathological concretions and tissue crystalline deposits. The comparison between IR spectra collected with conventional IR spectroscopy and IR spectra collected at the nanometer scale through OPT-IR may

show significant discrepancies depending on which chemical phase is investigated. Such differences exist for other spectroscopies such as AFM-IR or Raman spectroscopy and may have different origins.

In the case of pathologies related to cystine and DHA crystals, the signal to noise ratio is excellent and thus characterization at the nanometer scale

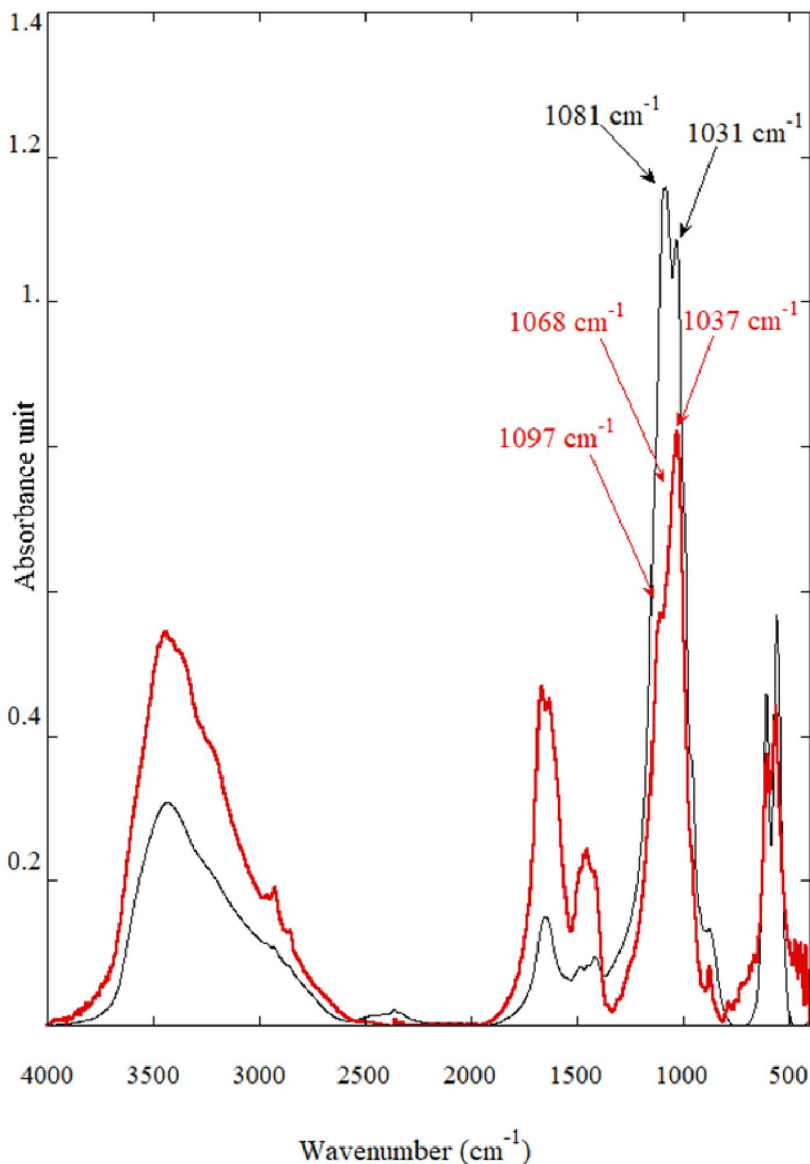


Figure 22. Classical FTIR spectra of calcium phosphate compounds identified in PMCD namely Wk (in black) with the splitting at 1081 and 1031 cm^{-1} and of a mixing of ACCP and CA (in red) with the shoulders at 1097 cm^{-1} (corresponding to CA) and 1068 cm^{-1} (corresponding to ACCP).

through IR spectroscopy can be considered for organic compounds. For the other chemical phases, namely minerals with broad IR absorption bands, such characterization seems to be more difficult. Let's recall also that a shift (a few cm^{-1}) of IR bands for calcium oxalate may be associated to the presence of both COD and COM (underlining that the patient suffers from hyperoxaluria (linked to the presence

of COM) and hypercalciuria (linked to the presence of COD). One problem comes from the possibility to distinguish between different calcium phosphate compounds which is clearly a limitation in the case of breast calcification.

Complementary experiments are ongoing to clearly define the origin of the discrepancy which can exist for different chemical phases identified

in pathological calcifications between conventional μ FTIR and OPT-IR spectroscopy.

Conflicts of interest

Authors have no conflict of interest to declare.

References

- [1] D. Bazin, M. Daudon, C. Combes, C. Rey, *Chem. Rev.*, 2012, **112**, 5092-5120.
- [2] D. Bazin, M. Daudon, *J. Phys. D: Appl. Phys.*, 2012, **45**, article no. 383001.
- [3] L. N. Poloni, M. D. Ward, *Chem. Mater.*, 2014, **26**, 477-495.
- [4] D. Bazin, M. Daudon, *Ann. Biol. Clin.*, 2015, **73**, 517-534.
- [5] E. Tsolaki, S. Bertazzo, *Materials*, 2019, **12**, article no. 3126.
- [6] D. Bazin, E. Letavernier, J. P. Haymann, V. Frochot, M. Daudon, *Ann. Biol. Clin.*, 2020, **78**, 349-362.
- [7] D. Bazin, M. Daudon, V. Frochot, J.-Ph. Haymann, E. Letavernier, *C. R. Chim.*, 2022, **25**, no. S1, 133-147.
- [8] A. Ben Lakhdar, M. Daudon, M. C. Matthieu, A. Kellum, C. Balleyguier, D. Bazin, *C. R. Chim.*, 2016, **19**, 1610-1624.
- [9] R. Scott, C. Kendall, N. Stone, K. Rogers, *Sci. Rep.*, 2017, **7**, article no. 136.
- [10] J. A. M. R. Kunitake, S. Choi, K. X. Nguyen, M. M. Lee, F. He, D. Sudilovsky, P. G. Morris, M. S. Jochelson, C. A. Hudis, D. A. Muller, P. Fratzl, C. Fischbach, A. Masi, L. A. Estroff, *J. Struct. Biol.*, 2018, **202**, 25-34.
- [11] P. Dorfmüller, D. Bazin, S. Aubert, R. Weil, F. Brisset, M. Daudon, F. Capron, I. Brocheriou, *Cardiol. Res. Pract.*, 2010, **2010**, article no. 685926.
- [12] R. Coscas, M. Bensussan, M.-P. Jacob, L. Louedec, Z. Massy, J. Sadoine, M. Daudon, C. Chaussain, D. Bazin, J.-B. Michel, *Atherosclerosis*, 2017, **259**, 60-67.
- [13] A. P. Sage, Y. Tintut, L. L. Demer, *Nat. Rev. Cardiol.*, 2010, **7**, 528-536.
- [14] X. Carpentier, M. Daudon, O. Traxer, P. Jungers, A. Mazouyes, G. Matzen, E. Véron, D. Bazin, *Urology*, 2009, **73**, 968-975.
- [15] D. Bazin, G. André, R. Weil, G. Matzen, E. Véron, X. Carpentier, M. Daudon, *Urology*, 2012, **79**, 786-790.
- [16] R. Flannigan, W. H. Choy, B. Chew, D. Lange, *Nat. Rev. Urol.*, 2014, **11**, 333-341.
- [17] E. J. Espinosa-Ortiz, B. H. Eisner, D. Lange, R. Gerlach, *Nat. Rev. Urol.*, 2019, **16**, 35-53.
- [18] M. Daudon, M. Petay, S. Vimont, A. Denizet, F. Tielens, J.-Ph. Haymann, E. Letavernier, V. Frochot, D. Bazin, *C. R. Chim.*, 2022, **25**, no. S1, 315-334.
- [19] D. Bazin, R. J. Papoular, E. Elkaim, R. Weil, D. Thiaudière, C. Pisapia, B. Ménez, N. S. Hwang, F. Tielens, M. Livrozet, E. Boudierlique, J.-Ph. Haymann, E. Letavernier, L. Hennem, V. Frochot, M. Daudon, *C. R. Chim.*, 2022, **25**, no. S1, 343-354.
- [20] P. Cochat, G. Rumsby, *New Engl. J. Med.*, 2013, **369**, 649-658.
- [21] M. Daudon, P. Jungers, D. Bazin, *New Engl. J. Med.*, 2008, **359**, 100-102.
- [22] A. Dessombz, E. Letavernier, J.-Ph. Haymann, D. Bazin, M. Daudon, *J. Urol.*, 2015, **193**, 1564-1569.
- [23] J. R. M. Oliveira, M. F. Oliveira, *Sci. Rep.*, 2016, **6**, article no. 22961.
- [24] E. Boudierlique, E. Tang, J. Perez, H.-K. Ea, F. Renaudin, A. Coudert, S. Vandermeersch, D. Bazin, J.-Ph. Haymann, C. Saint-Jacques, V. Frochot, M. Daudon, E. Letavernier, *C. R. Chim.*, 2022, **25**, no. S1, 393-405.
- [25] D. Bazin, M. Rabant, J. Mathurin, M. Petay, A. Denizet-Besseau, A. Dazzi, Y. Su, E. P. Hessou, F. Tielens, F. Borondics, M. Livrozet, E. Boudierlique, J.-Ph. Haymann, E. Letavernier, V. Frochot, M. Daudon, *C. R. Chim.*, 2022, **25**, no. S1, 489-502.
- [26] F. Meiouet, S. El Kabbaj, M. Daudon, *C. R. Chim.*, 2022, **25**, no. S1, 281-293.
- [27] H. Colboc, Ph. Moguelet, E. Letavernier, V. Frochot, J.-F. Bernaudin, R. Weil, S. Rouzière, P. Seneth, C. Bachmeyer, N. Laporte, I. Lucas, V. Descamps, R. Amodek, F. Brunet-Possentik, N. Kluger, L. Deschamps, A. Dubois, S. Reguer, A. Somogyi, K. Medjoubi, M. Refregiers, M. Daudon, D. Bazin, *C. R. Chim.*, 2022, **25**, no. S1, 445-476.
- [28] G. Chebion, E. Bugni, V. Gerin, M. Daudon, V. Castiglione, *C. R. Chim.*, 2022, **25**, no. S1, 295-306.
- [29] M. Daudon, V. Frochot, D. Bazin, P. Jungers, *Drugs*, 2018, **78**, 163-201.
- [30] A. Trinchieri, *Arch. Ital. Urol. Androl.*, 1996, **68**, 203-250.
- [31] M. Daudon, B. Knebelmann, *Rev. Prat.*, 2011, **61**, 372-378.
- [32] I. Sorokin, C. Mamoulakis, K. Miyazawa, A. Rodgers, J. Talati, Y. Lotan, *World J. Urol.*, 2017, **35**, 1301-1320.
- [33] Y. Liu, Y. Chen, B. Liao, D. Luo, K. Wang, H. Li, G. Zeng, *Asian J. Urol.*, 2018, **5**, 205-214.
- [34] A. Trinchieri, *Clin. Cases Miner. Bone Metab.*, 2008, **5**, 101-106.
- [35] M. Daudon, C. A. Bader, P. Jungers, *Scanning Microsc.*, 1993, **7**, 1081-1104.
- [36] M. Daudon, *Arch. Pédiatr.*, 2000, **7**, 855-865.
- [37] M. Daudon, P. Jungers, *Nephron Physiol.*, 2004, **98**, 31-36.
- [38] M. Daudon, P. Jungers, D. Bazin, *AIP Conf. Proc.*, 2008, **1049**, 199-215.
- [39] M. Daudon, H. Bouzidi, D. Bazin, *Urol. Res.*, 2010, **38**, 459-467.
- [40] M. Daudon, A. Dessombz, V. Frochot, E. Letavernier, J.-Ph. Haymann, P. Jungers, D. Bazin, *C. R. Chim.*, 2016, **19**, 1470-1491.
- [41] J. C. Williams Jr., G. Gambaro, A. Rodgers, J. Asplin, O. Bonny, A. Costa-Bauzá, P. M. Ferraro, G. Fogazzi, D. G. Fuster, D. S. Goldfarb, F. Grases, I. P. Heilberg, D. Kok, E. Letavernier, G. Lippi, M. Marangella, A. Nouvenne, M. Petrarulo, R. Siener, H.-G. Tiselius, O. Traxer, A. Trinchieri, E. Croppi, W. G. Robertson, *Urolithiasis*, 2021, **49**, 1-16.
- [42] G. Herzberg, *Molecular Spectra and Molecular Structure. Vol. 2: Infrared and Raman Spectra of Polyatomic Molecules*, Van Nostrand, Reinhold, New York, 1945.
- [43] H. Humecki, *Practical Applications of Infrared Microspectroscopy*, Marcel Dekker, Inc., New York, 1995.
- [44] D. C. Fernandez, R. Bhargava, S. M. Hewitt, I. W. Levin, *Nat. Biotechnol.*, 2005, **23**, 469-474.
- [45] L. M. Miller, P. Dumas, *Biochim. Biophys. Acta – Biomembr.*, 2006, **1758**, 846-857.
- [46] L. Maurice-Estépa, P. Levillain, B. Lacour, M. Daudon, *Scand. J. Urol. Nephrol.*, 1999, **33**, 299-305.
- [47] L. Estépa, M. Daudon, *Biospectroscopy*, 1997, **3**, 347-369.
- [48] M. Daudon, D. Bazin, *C. R. Chim.*, 2016, **19**, 1416-1423.

- [49] D. Bazin, E. Letavernier, J.-Ph. Haymann, F. Tielens, A. Kellum, M. Daudon, *C. R. Chim.*, 2016, **19**, 1548-1557.
- [50] D. Nguyen Quy, M. Daudon, *Infrared et Raman Spectra of Calculi*, Elsevier, Paris, 1997.
- [51] M. Daudon, D. Bazin, K. Adil, A. Le Bail, *Acta Crystallogr. E*, 2011, **67**, article no. o1458.
- [52] A. Le Bail, D. Bazin, M. Daudon, A. Brochot, V. Robbez-Masson, V. Maisonneuve, *Acta Crystallogr. B*, 2009, **65**, 350-354.
- [53] D. Bazin, M. Daudon, E. Elkaim, A. Le Bail, L. Smrcok, *C. R. Chim.*, 2016, **19**, 1535-1541.
- [54] D. Bazin, Ch. Jouanneau, S. Bertazzo, Ch. Sandt, A. Desombz, M. Réfrégiers, P. Dumas, J. Frederick, J.-Ph. Haymann, E. Letavernier, P. Ronco, M. Daudon, *C. R. Chim.*, 2016, **19**, 1439-1455.
- [55] A. Dessombz, D. Bazin, P. Dumas, C. Sandt, J. Sule-Suso, M. Daudon, *PLoS One*, 2011, **6**, article no. e28007.
- [56] C. Petibois, M. Piccinini, M. C. Guidi, A. Marcelli, *J. Synchrotron Radiat.*, 2010, **17**, 1-11.
- [57] M. J. Nasse, M. J. Walsh, E. C. Mattson, R. Reininger, A. Kajdacsy-Balla, V. Macias, R. Bhargava, C. J. Hirschmugl, *Nat. Methods*, 2011, **8**, 413-416.
- [58] A. M. Hanninen, R. C. Prince, R. Ramos, M. V. Plikus, E. O. Potma, *Biomed. Opt. Express*, 2018, **9**, 4807-4817.
- [59] A. Centrone, *Annu. Rev. Anal. Chem.*, 2015, **8**, 101-126.
- [60] G. L. Carr, *Rev. Sci. Instrum.*, 2001, **72**, article no. 1613.
- [61] A. Dazzi, F. Glotin, R. Carminati, *J. Appl. Phys.*, 2010, **107**, article no. 124519.
- [62] A. Dazzi, C. B. Prater, *Chem. Rev.*, 2017, **17**, 5146-5173.
- [63] D. Fournier, F. Lepoutre, A. Boccara, *J. Phys.*, 1983, **44**, 479-482.
- [64] Y. Luque, K. Louis, C. Jouanneau, S. Placier, E. Esteve, D. Bazin, E. Rondeau, E. Letavernier, A. Wolfrohm, C. Gosset, A. Boueilh, M. Burbach, P. Frère, M.-C. Verpont, S. Vandermeersch, D. Langui, M. Daudon, V. Frochot, L. Mesnard, *J. Am. Soc. Nephrol.*, 2017, **28**, 1723-1728.
- [65] E. Esteve, Y. Luque, J. Waeytens, D. Bazin, L. Mesnard, Ch. Jouanneau, P. Ronco, A. Dazzi, M. Daudon, A. Deniset-Besseau, *Anal. Chem.*, 2020, **92**, 7388-7392.
- [66] E. Esteve, "Applications des outils physicochimiques à la physiologie et physiopathologie rénale", PhD Thesis, Sorbonne University, Paris, France, 2021.
- [67] V. Castiglione, P.-Y. Sacré, E. Cavalier, P. Hubert, R. Gadsisseur, E. Ziemons, *PLoS One*, 2018, **13**, article no. e0201460.
- [68] I. Lucas, D. Bazin, M. Daudon, *C. R. Chim.*, 2022, **25**, no. S1, 83-103.
- [69] S. Tamosaityte, M. Pucetaite, A. Zelvy, S. Varvuolyte, V. Hendrixson, V. Sablinskas, *C. R. Chim.*, 2022, **25**, no. S1, 73-82.
- [70] M. Harada, K. Iwamoto, T. Kitamori, T. Sawada, *Anal. Chem.*, 1993, **65**, 2938-2940.
- [71] M. Kansiz, C. Prater, E. Dillon, M. Lo, J. Anderson, C. Marcott, A. Demissie, Y. Chen, G. Kunkel, *Microsc. Today*, 2020, **28**, 26-36.
- [72] D. Bazin, E. Boudierlique, M. Daudon, V. Frochot, J.-Ph. Haymann, E. Letavernier, F. Tielens, R. Weil, *C. R. Chim.*, 2022, **25**, no. S1, 37-60.
- [73] D. Bazin, M. Daudon, *J. Spectral Imaging*, 2019, **8**, article no. a16.
- [74] M. Daudon, D. Bazin, "New techniques to characterize kidney stones and Randall's plaque", in *Urolithiasis: Basic Science and Clinical Practice* (J. J. Talati, H. G. Tiselius, D. M. Albala, Z. Ye, eds.), Springer, Berlin, 2012, 683-707.
- [75] M. Toplak, S. T. Read, C. Sandt, F. Borondics, *Cells*, 2021, **10**, article no. 2300.
- [76] N. E. Olson, Y. Xiao, Z. Lei, A. P. Ault, *Anal. Chem.*, 2020, **92**, 9932-9939.
- [77] N. Baden, H. Kobayashi, N. Urayama, *Int. J. Polym. Anal. Character.*, 2020, **25**, 1-7.
- [78] V. Beltran, A. Marchetti, G. Nuyts, M. Leeuwestein, Ch. Sandt, F. Borondics, K. De Wael, *Angew. Chem. Int. Ed. Eng.*, 2021, **60**, 22753-22760.
- [79] A. J. Wang, E. P. Dillon, S. Maharjan, K.-S. Liao, B. P. McElhenny, T. Tong, S. Chen, J. Bao, S. A. Curran, *Adv. Mater. Interfaces*, 2021, **8**, article no. 2001720.
- [80] M. Kansiz, L. M. Dowling, I. Yousef, O. Guaitella, F. Borondics, J. Sulé-Suso, *Anal. Chem.*, 2021, **93**, 11081-11088.
- [81] N. Gustavsson, A. Paulus, I. Martinsson, A. Engdahl, K. Medjoubi, K. Klementiev, A. Somogyi, T. Deierborg, F. Borondics, G. K. Gouras, O. Klementieva, *Light: Sci. Appl.*, 2021, **10**, article no. 151.
- [82] G. Bakir, B. E. Girouard, R. Wiens, S. Mastel, E. Dillon, M. Kansiz, K. M. Gough, *Molecules*, 2020, **25**, article no. 4295.
- [83] C. Lima, H. Muhamadali, Y. Xu, M. Kansiz, R. Goodacre, *Anal. Chem.*, 2021, **93**, 3082-3088.
- [84] A. Spadea, J. Denbigh, M. J. Lawrence, M. Kansiz, P. Gardner, *Anal. Chem.*, 2021, **93**, 3938-3950.
- [85] P. Zhao, Y. Zhao, L. Cui, Y. Tian, Z. Zhang, Q. Zhu, W. Zhao, *Sci. Total Environ.*, 2021, **775**, article no. 145846.
- [86] D. Khanal, J. Zhang, W.-R. Ke, M. M. Banaszak Holl, H.-K. Chan, *Anal. Chem.*, 2020, **92**, 8323-8332.
- [87] D. Zhang, C. Li, C. Zhang, M. N. Slipchenko, G. Eakins, J.-X. Cheng, *Sci. Adv.*, 2016, **2**, article no. e1600521.
- [88] O. Klementieva, Ch. Sandt, I. Martinsson, M. Kansiz, G. K. Gouras, F. Borondics, *Adv. Sci.*, 2020, **7**, article no. 1903004.
- [89] T. Echigo, M. Kimata, A. Kyono, M. Shimizu, T. Hatta, *Mineral. Mag.*, 2005, **69**, 77-88.
- [90] M. Daudon, D. Bazin, G. Andre, P. Jungers, A. Cousson, P. Chevallier, E. Véron, G. Matzen, *J. Appl. Crystallogr.*, 2009, **42**, 109-115.
- [91] I. Petit, G. D. Belletti, Th. Debroise, M. J. Llanosola-Portoles, I. T. Lucas, C. Leroy, Ch. Bonhomme, L. Bonhomme-Coury, D. Bazin, M. Daudon, E. Letavernier, J. Ph. Haymann, V. Frochot, F. Babonneau, P. Quaino, F. Tielens, *Chemistry Select*, 2018, **3**, 8801-8812.
- [92] C. Conti, L. Brambilla, Ch. Colombo, D. Dellasega, G. Diego Gatta, M. Realini, G. Zerbi, *Phys. Chem. Chem. Phys.*, 2010, **12**, 14560-14566.
- [93] Q. Liu, S. Huang, J. P. Matinlinna, Zh. Chen, H. Pan, *BioMed Res. Int.*, 2013, **2013**, article no. 929748.
- [94] Ch. Combes, S. Cazalbou, Ch. Rey, *Minerals*, 2016, **6**, 1-25.
- [95] D. Bazin, C. Chappard, C. Combes, X. Carpentier, S. Rouzière, G. André, G. Matzen, M. Allix, D. Thiaudière, S. Reguer, P. Jungers, M. Daudon, *Osteoporos. Int.*, 2009, **20**, 1065-1075.
- [96] X. Carpentier, D. Bazin, P. Jungers, S. Reguer, D. Thiaudière, M. Daudon, *J. Synchrotron Radiat.*, 2010, **17**, 374-379.
- [97] J. Mathurin, A. Deniset-Besseau, D. Bazin, E. Dartois, M. Wagner, A. Dazzi, *J. Appl. Phys.*, 2022, **131**, article no. 010901.

- [98] T. Alelign, B. Petros, *Adv. Urol.*, 2018, **2018**, article no. 3068365.
- [99] F. L. Coe, A. E. Evan, E. Worcester, *J. Clin. Investig.*, 2005, **115**, 2598-2608.
- [100] A. Guerra, A. Ticinesi, F. Allegri, S. Pinelli, R. Aloe, T. Meschi, *Urolithiasis*, 2020, **48**, 271-279.
- [101] T. Debroise, T. Sedzik, J. Vekeman, Y. Y. Su, Ch. Bonhomme, F. Tielens, *Cryst. Growth Design*, 2020, **20**, 3807-3815.
- [102] M. Shepelenko, Y. Feldman, L. Leiserowitz, L. Kronik, *Cryst. Growth Design*, 2020, **20**, 858-865.
- [103] A. V. Kustov, A. I. Strelnikov, *Urol. J.*, 2018, **15**, 87-91.
- [104] W. Zhao, N. Sharma, F. Jones, P. Raiteri, J. D. Gale, R. Demichelis, *Cryst. Growth Design*, 2016, **16**, 5954-5965.
- [105] A. Frey-Wyssling, *Am. J. Bot.*, 1981, **68**, 130-141.
- [106] A. Thomas, E. Rosseeva, O. Hochrein, W. Carillo-Cabrera, P. Simon, P. Duchstein, D. Zahn, R. Kniep, *Chem. Eur. J.*, 2012, **18**, 4000-4009.
- [107] A. Gehl, M. Dietzsch, M. Mondeshki, S. Bach, T. Häger, B. Barton, U. Kolb, W. Tremel, *Chem. Eur. J.*, 2015, **21**, 18192-18201.
- [108] M. Hajira, R. Graf, W. Tremel, *Chem. Commun.*, 2014, **50**, 6534-6536.
- [109] D. Bazin, C. Leroy, F. Tielens, Ch. Bonhomme, L. Bonhomme-Coury, F. Damay, D. Le Denmat, J. Sadoine, J. Rode, V. Frochot, E. Letavernier, J.-Ph. Haymann, M. Daudon, *C. R. Chim.*, 2016, **19**, 1492-1503.
- [110] M. Daudon, E. Letavernier, V. Frochot, J.-Ph. Haymann, D. Bazin, P. Jungers, *C. R. Chim.*, 2016, **19**, 1504-1513.
- [111] M. Daudon, *Ann. Urol.*, 2005, **39**, 209-231.
- [112] R. C. Walton, J. P. Kavanagh, B. R. Heywood, P. N. Rao, *J. Cryst. Growth*, 2005, **284**, 517-529.
- [113] M. Daudon, C. A. Bader, P. Jungers, *Scanning Microsc.*, 1993, **7**, 1081-1104.
- [114] M. Daudon, P. Junger, D. Bazin, *New Engl. J. Med.*, 2008, **359**, 100-102.
- [115] A. Lionet, M. Haeck, A. Garstka, V. Gnemmi, D. Bazin, E. Letavernier, J.-Ph. Haymann, Ch. Noel, M. Daudon, *C. R. Chim.*, 2016, **19**, 1542-1547.
- [116] P. Cartier, M. Hamet, *Clin. Chim. Acta*, 1968, **20**, 205-214.
- [117] G. Bollée, C. Dollinger, L. Boutaud, D. Guillemot, A. Bensman, J. Harambat, P. Deteix, M. Daudon, B. Knebelmann, I. Ceballos-Picot, *J. Am. Soc. Nephrol.*, 2010, **21**, 679-688.
- [118] B. Benedetto, R. Madden, A. Kurbanov, G. Braden, J. Freeman, G. S. Lipkowitz, *Am. J. Kidney Dis.*, 2001, **37**, E37.1-E37.4.
- [119] K. H. Fye, A. Sahota, D. C. Hancock, A. B. Gelb, J. Chen, J. W. Sparks, R. K. Sibley, J. A. Tischfield, *Arch. Internat. Med.*, 1993, **153**, 767-770.
- [120] D. Glicklich, H. E. Gruber, A. J. Matas, V. A. Tellis, G. Karwa, K. Finley, C. Salem, R. Soberman, J. Seegmiller, *Q. J. Med.*, 1988, **68**, 785-793.
- [121] L. Estepa-Maurice, C. Hennequin, C. Marfisi, C. Bader, B. Lacour, M. Daudon, *Am. J. Clin. Pathol.*, 1996, **105**, 576-582.
- [122] J. C. Williams Jr, J. E. Lingeman, M. Daudon, D. Bazin, *C. R. Chim.*, 2022, **25**, no. S1, 61-72.
- [123] P. Rueggsegger, B. Koller, R. Muller, *Calcif. Tissue Int.*, 1996, **58**, 24-29.
- [124] C. A. Zarse, J. A. McAteer, A. J. Sommer, S. C. Kim, E. K. Hatt, J. E. Lingeman, A. P. Evan, J. C. Williams Jr, *BMC Urol.*, 2004, **4**, article no. 15.
- [125] J. C. Williams Jr, J. A. McAteer, A. P. Evan, J. E. Lingeman, *Urol. Res.*, 2010, **38**, 477-484.
- [126] J. Harper, J. Lingeman, R. Sweet, I. Metzler, P. Sunaryo, J. C. Williams, A. Maxwell, J. Thiel, B. Cunitz, B. Dunmire, M. Bailey, M. D. Sorensen, *J. Urol.*, 2022, **207**, 1067-1076.
- [127] A. Randall, *Ann. Surg.*, 1937, **105**, 1009-1027.
- [128] M. Daudon, O. Traxer, P. Jungers, D. Bazin, *AIP Conf. Proc.*, 2007, **900**, 26-34.
- [129] M. Daudon, P. Jungers, D. Bazin, *AIP Conf. Proc.*, 2008, **1049**, 199-215.
- [130] M. Daudon, O. Traxer, J. C. Williams, D. Bazin, "Randall's plaques", in *Urinary Tract Stone Disease*, Springer, Berlin, 2010.
- [131] M. Daudon, D. Bazin, E. Letavernier, *Urolithiasis*, 2015, **43**, 5-11.
- [132] E. Letavernier, D. Bazin, M. Daudon, *C. R. Chim.*, 2016, **19**, 1456-1460.
- [133] S. Ohman, L. Larsson, *Med. Hypotheses*, 1992, **39**, 360-363.
- [134] A. Evan, J. Lingeman, F. L. Coe, E. Worcester, *Kidney Int.*, 2006, **69**, 1313-1318.
- [135] M. Daudon, D. Bazin, *J. Phys.: Conf. Ser.*, 2013, **425**, article no. 022006.
- [136] E. Letavernier, S. Vandermeersch, O. Traxer, M. Tligui, L. Baud, P. Ronco, J.-Ph. Haymann, M. Daudon, *Medicine (Baltimore)*, 2015, **94**, article no. e566.
- [137] D. Bazin, E. Letavernier, Ch. Jouanneau, P. Ronco, Ch. Sandt, P. Dumas, G. Matzen, E. Véron, J.-Ph. Haymann, O. Traxer, P. Conort, M. Daudon, *C. R. Chim.*, 2016, **19**, 1461-1469.
- [138] C. Verrier, D. Bazin, L. Huguet, O. Stéphan, A. Gloter, M.-Ch. Verpont, V. Frochot, J.-Ph. Haymann, I. Brocheriou, O. Traxer, M. Daudon, E. Letavernier, *J. Urol.*, 2016, **196**, 1566-1574.
- [139] E. Letavernier, G. Kauffenstein, L. Huguet, N. Navasiolava, E. Boudierlique, E. Tang, L. Delaitre, D. Bazin, M. de Frutos, C. Gay, J. Perez, M. C. Verpont, J.-Ph. Haymann, V. Pomozi, J. Zoll, O. Le Saux, M. Daudon, G. Leftheriotis, L. Martin, *J. Am. Soc. Nephrol.*, 2018, **29**, 2337-2347.
- [140] C. Gay, E. Letavernier, M.-Ch. Verpont, M. Walls, D. Bazin, M. Daudon, N. Nassif, O. Stephan, M. de Frutos, *ACS Nano*, 2020, **14**, 1823-1836.
- [141] S. R. Khan, B. K. Canales, P. R. Dominguez-Gutierrez, *Nat. Rev. Nephrol.*, 2021, **17**, 417-433.
- [142] S. R. Khan, *C. R. Chim.*, 2022, **25**, no. S1, 355-372.
- [143] E. Van de Perre, D. Bazin, V. Estrade, E. Boudierlique, K. M. Wissing, M. Daudon, E. Letavernier, *C. R. Chim.*, 2022, **25**, no. S1, 373-391.
- [144] X. Carpentier, D. Bazin, Ch. Combes, A. Mazouyes, S. Rouzière, P.-A. Albouy, E. Foy, M. Daudon, *J. Trace Elem. Med. Biol.*, 2011, **25**, 160-165.
- [145] R. F. Cox, M. P. Morgan, *Bone*, 2013, **53**, 437-445.
- [146] Y. V. Nalawade, *Indian J. Radiol. Imaging*, 2009, **19**, 282-286.
- [147] M. P. Morgan, M. M. Cooke, G. M. McCarthy, *J. Mammary Gland Biol. Neoplasia*, 2005, **10**, 181-187.
- [148] S. O'Grady, M. P. Morgan, *BBA - Rev. Cancer*, 2018, **1869**, 310-320.
- [149] P. Henrot, A. Leroux, C. Barlier, P. Génin, *Diagn. Interv. Imaging*, 2014, **95**, 141-152.

- [150] K. S. Shin, M. Laohajaratsang, S. Men, B. Figueroa, S. M. Dintzis, D. Fu, *Theranostics*, 2020, **10**, 5865-5878.
- [151] M. Petay, M. Cherfan, E. Boudierlique, S. Reguer, J. Mathurin, A. Dazzi, M. l'Heronde, M. Daudon, E. Letavernier, A. Deniset-Besseau, D. Bazin, *C. R. Chim.*, 2022, **25**, no. S1, 553-576.
- [152] S. Gosling, D. Calabrese, J. Nallala, Ch. Greenwood, S. Pinder, L. King, J. Marks, D. Pinto, Th. Lynch, I. D. Lyburn, E. S. Hwang, Grand Challenge PRECISION Consortium, K. Rogers, N. Stone, *Analyst*, 2022, **147**, 1641-1654.
- [153] M. J. Radi, *Arch. Pathol. Lab. Med.*, 1989, **113**, 1367-1369.
- [154] C. Tornos, E. Silva, A. El-Naggar, K. P. Pritzker, *Am. J. Surg. Pathol.*, 1990, **14**, 961-968.
- [155] L. D. Truong, J. Cartwright, L. Alpert, *Mod. Pathol.*, 1992, **5**, 146-152.
- [156] H. Poggi, H. C. W. Skinner, J. J. Ague, D. Carter, *Am. Mineral.*, 1998, **83**, 1122-1126.
- [157] R. Baker, K. D. Rogers, N. Shepherd, N. Stone, *Br. J. Cancer*, 2010, **103**, 1034-1039.
- [158] O. Hassler, *Cancer*, 1969, **23**, 1103-1109.
- [159] S. Gosling, R. Scott, C. Greenwood, P. Bouzy, J. Nallala, I. D. Lyburn, N. Stone, K. Rogers, *J. Mammary Gland Biol. Neoplasia*, 2019, **334**, 333-342.
- [160] E. Tsolaki, W. Doran, L. Magnani, A. Olivo, I. K. Herrmann, S. Bertazzo, 2021, bioRxiv preprint, <https://doi.org/10.1101/2020.04.29.067660>.
- [161] R. Vanna, C. Morasso, B. Marcinnò, F. Piccotti, E. Torti, D. Altamura, S. Albasini, M. Agozzino, L. Villani, L. Sorrentino, O. Bunk, F. Leporati, C. Giannini, F. Cors, *Cancer Res.*, 2020, **80**, 1762-1772.